

REMOTE DETECTION OF HYDROGEN LEAKS USING LASER INDUCED  
RAYLEIGH/MIE SCATTERING

By

SAMEER PARANJPE

A THESIS PRESENTED TO THE GRADUATE SCHOOL  
OF THE UNIVERSITY OF FLORIDA IN PARTIAL FULFILLMENT  
OF THE REQUIREMENTS FOR THE DEGREE OF  
MASTER OF SCIENCE

UNIVERSITY OF FLORIDA

2004

Copyright 2004

by

Sameer Subhash Paranjpe

## ACKNOWLEDGMENTS

The author would like to thank Dr. Jill Peterson for her guidance and support. I would also like to thank my fellow students Raghuram Vempati, Philip Jackson, Murray Fisher, Matthew Gabriel and Ryan Ferguson for their assistance in various portions of the project.

## TABLE OF CONTENTS

	<u>page</u>
ACKNOWLEDGMENTS .....	iii
LIST OF TABLES .....	vi
LIST OF FIGURES .....	vii
ABSTRACT .....	xi
CHAPTER	
1 INTRODUCTION .....	1
2 LITERATURE REVIEW .....	6
Mie Scattering .....	6
Rayleigh Scattering .....	7
Buoyant Jet Theory .....	9
3 THEORETICAL FRAMEWORK .....	10
Elastic and Inelastic Light Scattering .....	10
Elastic Scattering Mechanism .....	10
Mie Theory .....	11
Calculation of intensity distribution functions $I_1$ and $I_2$ .....	14
Rayleigh Theory .....	15
Photon arrival rate calculations for Rayleigh and Mie theory .....	17
Scattering Cross Section Considerations .....	18
Buoyant Jet Theory .....	18
Froude Number Calculation .....	19
Buoyant Jet Profiles and Concentration Variation .....	20
4 EXPERIMENTAL SCHEME .....	23
Collection at $90^\circ$ and Backscatter .....	23
Back Scatter Considerations .....	30
Data Recording Procedure .....	30

5	RESULTS AND DISCUSSION.....	32
	Comparison of Theoretical and Experimental Photon Arrival Rate.....	32
	Calculation of Theoretical Rayleigh Photon Arrival Rate.....	32
	Calculation of Theoretical Mie Photon Arrival Rate.....	33
	Calculation of Total Theoretical Photon Arrival Rate.....	38
	Calculation of Experimental Photon Arrival Rate.....	38
	Data Analysis Techniques.....	41
	Integrated area method.....	42
	Peak Voltage Method.....	43
	Analysis of Recorded Data.....	46
	Case I: Argon-ion laser.....	46
	Peak voltage variation.....	46
	Normalized peak voltage variation.....	48
	Standard deviation profiles.....	48
	Case II: Pulsed Nd:YAG laser ; pure helium.....	50
	Peak voltage variation.....	50
	Normalized Peak Voltage Variation.....	51
	Standard deviation profiles.....	51
	Case III: Pulsed Nd:YAG laser; 20%helium ,80% nitrogen.....	52
	Peak voltage variation.....	52
	Normalized peak voltage variation.....	53
	Standard Deviation Profiles.....	54
	Measurements in Backscatter.....	55
6	CONCLUSIONS.....	58
	LIST OF REFERENCES.....	60
	BIOGRAPHICAL SKETCH.....	62

## LIST OF TABLES

<u>Table</u>	<u>page</u>
3-1 Scattering cross section at a wavelength of 532 nm.....	18
3-2 Froude number calculations show that the criteria for buoyant jet is met for all combinations of flow fluids, nozzle diameters and downstream distances.....	20
5-1 Particle counter data show the particle distribution in the lab .....	34
5-2 Shows that average peak voltage recorded after 300 pulses in shear layer is a converged mean.....	45
5-3 Control volume to leak diameter ratio for all three cases shows that the ratio is far less for backscatter than 90° scattering .....	57

## LIST OF FIGURES

<u>Figure</u>	<u>page</u>
3-1 Mie scattering geometry.....	11
3-2 $I_1$ (perpendicular) and $I_2$ (parallel) intensity distribution functions from the interactive webpage.....	15
3-3 $I_1$ (perpendicular) and $I_2$ (parallel) intensity distribution functions from McCartney.....	15
3-4 Instantaneous and time averaged profiles of a typical buoyant jet.....	21
3-5 Concentration variation with $r$ for $z = 2$ .....	22
4-1 Experimental scheme for collection of scattered light at $90^\circ$ .....	24
4-2 Experimental scheme for collection of scattered light at a $180^\circ$ (back scatter).....	25
4-3 Nozzle mounting showing three dimensional motion capability.....	27
4-3 Photomultiplier tube linearity tested as a function of flash lamp voltage.....	29
4-4 Calculation of nozzle traverse distances.....	31
5-1 Theoretical photon arrival rate calculations.....	33
5-2 Model M shows maritime distribution of aerosols (McCartney 1979, page 139).....	35
5-3 Model M duplicated on a log-normal scale.....	36
5-4 Comparison of number density of maritime and lab aerosols.....	37
5-5 Effect of maritime and lab aerosol distribution on Mie scattered intensity.....	37
5-6 Typical waveform of a burst seen on the oscilloscope.....	39
5-7 Points in shear layer where measurements are made.....	40
5-8 Comparison of experimental and theoretical photon arrival rates.....	41
5-9 Convergence studies of normalized area and averaged area.....	42

5-10	Waveform with varying glare at four downstream locations.....	43
5-11	All four waveforms normalized with their individual peaks.....	44
5-12	Voltage variation for Argon-Ion laser.....	47
5-13	Normalized peak voltage variation for argon-ion laser.....	48
5-14	Percent standard deviation variation for near field case.....	49
5-15	Percent standard deviation for far field case.....	49
5-16	Voltage variation for pulsed Nd:YAG laser.....	50
5-17	Normalized peak voltage variation for Nd:YAG laser.....	51
5-18	Standard deviation variation for Nd:YAG laser for pure helium.....	52
5-19	Relative size of beam and leak diameter.....	52
5-20	Voltage variation for the pulsed Nd:YAG laser for the mixture.....	53
5-21	Normalized peak voltage variation for Nd:YAG laser for the mixture.....	54
5-22	Percent standard deviation variation for Nd:YAG laser for the mixture of helium and nitrogen to simulate the optical properties of nitrogen.....	54
5-23	Schematic of backscatter on a time basis shows separation between beam dump glare and scattered signal from the nozzle.....	55
5-24	Normalized area variation shows a reduction in scattered intensity in presence of helium (backscatter); Nozzle diameter = $\frac{1}{4}$ " ; Re =500; Fr = 290.....	56

## NOMENCLATURE

$a$  = particle radius (m)

$C$  = concentration of the flow fluid ( $\text{kg}/\text{m}^3$ )

$C^*$  = dimensionless density

$C_{\text{PMT}}$  = photomultiplier tube calibration constant

$D$  = diameter of the nozzle (m ; ")

$E^i$  = Electric vector of the incident wave (V/m)

$Fr$  = Froude number =  $Re/Gr^2$

$G$  = gravitational acceleration ( $\text{m}/\text{s}^2$ )

$Gr$  = Grashof number =  $g(\rho_a - \rho_o)D^3/\rho_o\nu$

$H^i$  = Magnetic vector of the incident wave (N/Ampere-m)

$I_o$  = Incident laser power (W; photons/pulse)

$l$  = length of control volume (m)

$m$  = mass flow rate ( $\text{kg}/\text{s}$ )

$n$  = gas index of refraction at known reference conditions

$n(r)$  = number density per radius interval ( $\text{molecules}/\text{m}^3/\text{micron}$ )

$N$  = molecular number density ( $\text{molecules}/\text{m}^3$ )

$N_d$  = number of data points.

$r$  = radial distance from jet centerline (m)

$r_{x-y}$  = cross co-relation coefficient

$Re$  = Reynolds number =  $\rho\nu D/\mu = 4m/\pi D\mu$

$v$  = velocity of buoyant jet (m/s)

$V$  = photomultiplier tube voltage (V)

$x$  = percent helium

$y$  = distance from jet centerline normal to beam

$z$  = downstream distance (mm)

### **Greek Symbols**

$\alpha$  = size parameter =  $2\pi a/\lambda$

$\beta$  = spread angle

$\theta$  = angle of observation measured from the forward to scattering directions.

$\varphi$  = scattering angle

$\psi$  = wave function

$\eta$  = optical efficiency of transmitting and collecting lenses

$\Omega$  = solid angle of the collection optics

$\lambda$  = wavelength of laser light (nm)

$\sigma$  = differential scattering cross section ( $\text{m}^2/\text{sr}$ )

$\rho$  = density of gas ( $\text{kg}/\text{m}^3$ )

$\mu$  = dynamic viscosity of gas (Pa-s)

$\nu$  = dynamic viscosity of gas

### **Subscripts**

a = ambient

cl = centerline

i = species

m = mixture

o = jet exit condition

Abstract of Thesis Presented to the Graduate School  
of the University of Florida in Partial Fulfillment of the  
Requirements for the Degree of Master of Science

REMOTE DETECTION OF HYDROGEN LEAKS USING LASER INDUCED  
RAYLEIGH/MIE SCATTERING

By

Sameer Paranjpe

December 2004

Chair: Jill Peterson

Major Department: Mechanical and Aerospace Engineering

The current study examines the use of laser induced Rayleigh/Mie scattering as a means of remotely detecting hydrogen leaks. An axisymmetric vertical buoyant jet at a Reynolds number of 500 was used to simulate the hydrogen leak and the scattered signal indicating hydrogen concentration was examined at different downstream locations. Helium was used as a substitute for hydrogen for safety reasons. The scattering cross section of hydrogen is 0.23 times the scattering cross section of air and the scattering cross section of helium is 0.015 times the scattering cross section of air. A mixture of 20% helium and 80% nitrogen was also used at the same Reynolds number of 500, since the scattering cross section of this mixture equals the scattering cross section of hydrogen. The principal challenges in RLS detection were electronic shot noise and Mie scattering. The electronic shot noise was found to induce less than 0.1% uncertainty for an averaging time of 1 second. A Nd:YAG pulse laser operating at a wavelength of 532 nm was used and the scattered signal from the helium leak was collected at 90 to the

incident beam and focused onto a photomultiplier tube. The signal from the photomultiplier tube was read through a high speed digital oscilloscope. The repeatability and reproducibility of the data was established using a set of convergence studies. It was found that the amplitude of the Rayleigh/Mie signal decreased by 25% and the standard deviation increased by 45% in the presence of helium. This increase in standard deviation is more than the established values of 305. Non dimensionalized profiles collapsed to a classic similar shape, further documenting experimental results.

## CHAPTER 1 INTRODUCTION

Hydrogen is an attractive fuel source. However, leak detection is essential if it is to become a widespread, easily used and safe source of energy. It is relatively simple to determine whether a system is leaking hydrogen by identifying pressure drops. Finding the source of the leak however can be time consuming, costly and dangerous. The conventional method of leak detection involves the use of contact sensors. The following are the typical varieties of contact sensors commonly used for leak detection.

**Catalytic bead sensors.** These sensors consist of two beads surrounding a wire operating at a temperature of around 450°C. One of the beads is passivated. This ensures that it does not react with gas molecules. The other bead is coated with a catalyst to promote a reaction with the gas. The beads are generally placed on separate legs of a Wheatstone bridge circuit. When hydrogen is present, there is no measurable effect on the passivated bead, but there is a significant effect on the catalyzed bead. The increase in heat increases the resistance in that leg of the Wheatstone bridge circuit, which in turn changes the bridge balance signal, and this serves as the sensor signal. These sensors are usually used in the 1 to 5 % hydrogen range. The response time of the sensor varies, ranging from 10 to 30 seconds for full-scale response.

**Semiconductor sensors.** These sensors use semiconducting oxides whose electrical resistance changes in the presence of hydrogen due to a reduction reaction. These sensors generally operate at temperatures above ambient. The disadvantage of these sensors is that the oxides change their resistance as the oxygen concentration in the

environment changes, making these sensors unsuitable for such environments. They have a fast response time and detection limits of 0-1000 ppm hydrogen.

**Electrochemical sensors.** Electrochemical sensors are composed of an anode and cathode sandwiching a chemically sensitive electrolyte. When hydrogen passes over the electrolyte, a reversible chemical reaction occurs. This generates a current proportional to the gas concentration. However, oxygen is required to ensure chemical reversibility. This implies that the sensor is not environmentally independent. Electrochemical sensors are typically used to detect hydrogen in the range of 100 to 1000 ppm. Response times can be as low as several seconds, although typically these sensors are specified at 30 to 50 seconds for full-scale response.

**Resistive palladium alloy sensors.** The surface of palladium acts catalytically to break the H-H bond in diatomic hydrogen and allows the monatomic hydrogen to diffuse into the material. Palladium can dissolve more than 600 times its volume in hydrogen. The level of dissolved hydrogen proportionally changes the electrical resistivity of the metal. No other gases or environmental controls are necessary for these measurements.

**Hydrogen field effect transistor.** By using palladium as the gate material for a standard field effect transistor, small changes in the resistivity of the palladium produce large changes in the current-voltage characteristics of the FET. This sensor technology works well in the range of 50 to 1000 ppm range of hydrogen.

Although all these systems can effectively detect hydrogen leaks, the sensors are intrusive and have to be physically inserted into the suspect area. However due to the low combustion limits (4%) of hydrogen, for safety issues in most applications, it would be

advantageous if the leak could be detected without actually inserting a probe in the suspected area. The current study explores a novel remote detection technique.

### **Laser Induced Rayleigh/Mie Scattering**

This method uses a laser directed at a suspected leak source. As the laser pulse moves through air, the electromagnetic wave interacts with aerosols in the atmosphere and the molecules of the component gases. This causes some of the incident laser light to scatter in all directions, with varying intensities depending on the particle type and size. Substantial information can then be obtained by looking at the intensity of scattered light. The principal advantages of this technique are that it is non intrusive, it does not alter the flow pattern, and it has high spatial and temporal resolution.

Almost 99% of the light scattered by atmospheric particles is elastically scattered. Rayleigh and Mie scattering are the two types of elastic light scattering theories. The mechanism of elastic light scattering and the quantification of the scattering cross section and scattered intensity terms are dealt in Chapter 3. Mie theory was developed by the German physicist G. Mie (1908). It is in terms of complex series solutions and is valid for particles of all sizes. If the particle size becomes very large, then Mie theory can be simplified using geometric optics. However, for particles with a diameter much less (approximately 0.06 times or less) than the wavelength of incident light, the Mie theory reduces to a single term simplification called the Rayleigh theory. The amount of light a particular particle can scatter can be defined in terms of its scattering cross section. Thus a particle with a higher scattering cross section would scatter more light than a particle with a lower scattering cross section. For Rayleigh/Mie scattering, the scattering cross section is a dominant function of the particle size, wavelength of incident light and refractive index of the particle. The scattering cross section of hydrogen is about  $1/5^{\text{th}}$  that

of the surrounding air molecules. Hence the intensity of light scattered by hydrogen is expected to be less than the intensity of light scattered by the surrounding air molecules. In the absence of hydrogen, there would be a steady signal from the atmosphere that would consist of the Mie signal from the aerosols and Rayleigh signal from the air molecules. In the presence of hydrogen, we should expect this signal to fall.

The primary objective of this study is to detect the fall in scattered intensity in the presence of hydrogen. Because of safety issues, helium, which has a scattering cross-section 0.015 times that of air is used for the experimentation. In order to match the scattering cross section of hydrogen, a mixture of 20% helium and 80% nitrogen is also used. The scattered intensity is directly proportional to the scattering cross section. The proportionality constant depends on the experimental conditions. For a fixed experimental set up, the scattered signal from a given control volume would be the same if the product of scattering cross section and number density of species in that control volume is identical. Hence, as seen in Chapter 3, the scattered signal from a mixture of 20% helium and 80% nitrogen and from pure hydrogen are the same.

A second objective is to test the limits of detection. The measurements are taken at four different downstream locations for this purpose. Also measurements are taken in back scatter to test the feasibility of the technique for field measurements.

Two nozzles with diameters of  $\frac{1}{4}$ " (6.3mm) and  $\frac{1}{2}$ " (12.6mm) are used for simulating the leak. A continuous wave low power argon ion laser is used with the  $\frac{1}{4}$ " nozzle and a high power pulsed Nd:YAG laser was used with the  $\frac{1}{2}$ " nozzle. For each nozzle diameter the data is recorded for the two cases of pure helium and the mixture of 20% helium and 80% nitrogen. The Reynolds number is fixed at 500 for each case and

Froude numbers are calculated as discussed in Chapter 3. For all combinations of Reynolds and Froude numbers the leak is an axisymmetric vertical buoyant jet. The mean and fluctuating temperature and concentration profiles of a buoyant jet are well established. Since the leak is a buoyant jet it is expected that the variation of recorded scattered voltage would follow these profiles.

## CHAPTER 2 LITERATURE REVIEW

### **Mie Scattering**

Mie theory is the general solution for scattering of a plane electromagnetic wave by a particle of arbitrary size. In 1908 Mie first derived the relations for calculating various scattering characteristics of electromagnetic radiation, by homogenous, absorbing spheres of any diameter. The Mie solution was obtained via the solution of the wave equation which originates from the more fundamental Maxwell relations. The details of the Mie solution from these basic equations have been dealt with in references such as Kerker (1969), and Bohren and Huffman (1983).

The solution involves series expansions called the angular intensity distribution functions. These distribution functions are complex and involve the calculation of Legendre polynomials and Riccati-Bessel functions. Over the past 30 years numerous algorithms and subroutines have been developed mostly in FORTRAN and C to calculate these functions. The first subroutine for calculating the scattering functions was developed by Dave (1970) and incorporates the first 10 terms of the series expansion. Wiscombe (1980) developed algorithms for calculating the intensity distribution functions. These functions were plotted as a function of scattering angle and were robust for any given combination of particle size, incident wavelength and refractive index. An interactive webpage was developed by Prahl (2000) which allows the computation of the intensity distribution functions at any value of scattering angle for input values of incident wavelength, particle size and refractive index. This subroutine is used for the

theoretical calculations of Mie scattered intensity in this study. The results of the subroutine are verified against published values of the angular intensity distribution functions in Kerker (1969). The comparison is discussed in Chapter 3. McCartney (1976) lists standard aerosol distribution for continental and maritime distributions. Using these particle distributions, the number of particles of a particular size can be calculated as discussed in Chapter 5. Knowing the particle size distribution, the intensity distribution functions can be calculated using the subroutine by Prah1 (2000). The details of these calculation are shown in Chapter 5.

Mie scattering from particles has been used as a probe for monitoring concentration fluctuations. This technique called Marker nephelometry uses light scattered from seeded particles in a flow (Mie scatters) as a concentration probe. Since its introduction in 1961 by Rosenweig et al. (1961), this technique has proven to be a very useful probe for monitoring real time fluctuations manifested by seeded particles in the flow. Becker et al.(1967) and Shaughnessy and Morton (1977) have described the application of this technique. The same technique has been used for 2-D measurements by Long et al.(1981). These workers used a plane of light to illuminate particles in a flow field and used a television camera to get a digitized 2-D image of turbulent mixing.

### **Rayleigh Scattering**

For particles smaller than the incident wavelength (diameter  $< 0.06$  wavelength) only the first term of the Mie solution is needed to predict the intensity of scattered light. This single term simplification called the Rayleigh theory has been extensively discussed in literature notably by McCartney (1976) and Kerker (1969). Van de Hulst (1981) addressed the issue of assuming Rayleigh scattering to be single and independent of surrounding scatters. At 1 atm pressure and at a temperature of 300 K, air molecules are

separated by distances over 600 radii. He estimated that 3 radii distance between surrounding scatters is sufficient separation to ensure independent scattering. This means that the assumption of no multiple scattering is valid for air molecules for pressures much higher than atmospheric pressures.

Rayleigh light scattering is an ideal probe for gas temperature and concentration measurements since it is non-obtrusive, direct and has high spatial and temporal resolution. Using the Rayleigh scattered signal the number density of species under consideration can be calculated and since for an ideal gas at constant pressure, the number density is inversely proportional to temperature, the temperature can be known. Using this relation Muller-Dethelfs and Weinberg (1979) first used Rayleigh light scattering for temperature measurements in flame speed experiments. Dibble et al. (1980) used this technique to measure temperature fluctuations in premixed flames and also demonstrated that this technique could be extended to turbulent diffusion flames where the fuel and air have been carefully chosen to have identical Rayleigh scattering cross sections. Pitz et al. (1976) use RLS to measure temperature in a hydrogen-air flame. Horton and Peterson (1999) carried out transient temperature measurements in an ideal gas using laser induced RLS. Flow visualizations and transient temperature measurements were done in an axisymmetric impinging jet in a rapid thermal chemical vapor deposition reactor using RLS by Matthew and Peterson (2002). Robben (1975) evaluated the spectral broadening of Rayleigh scattered light to derive a temperature in turbulent flow measurements. Rayleigh light scattering has also been used for monitoring the concentration fluctuations which occur in isothermal turbulent flows by Graham et al.

(1974) and Dyer (1979). Pitts and Kashiwagi (1983) used RLS for the study of turbulent mixing. Bryner and Pitts (1992) used RLS for combustion studies.

One of the major disadvantages of RLS is background glare, which is at the same wavelength as that of the scattered beam and is impossible to filter from the signal. Glare minimization is possible by blackening the surfaces. Otugen (1993) used a dual line detection RLS technique for gas temperature measurements in which they eliminated surface scattered laser light from the Rayleigh signal by using two wavelengths. A primary assumption in this study was that the ratio of the surface reflection at two wavelengths is constant. The results indicated that accurate temperature measurements were possible even when the laser light background intensity was twice the Rayleigh signal.

### **Buoyant Jet Theory**

As previously stated, in this study the leak is created using pure helium and a mixture of 20% helium and 80% nitrogen. The density of both pure helium and the mixture of helium and nitrogen is different from the surrounding fluid (air). The Reynolds number is set at 500. As discussed in Chapter 3 the leak for both cases could be assumed to be an axisymmetric vertical buoyant jet. The mean and fluctuating temperature and concentration profiles of a buoyant jet are well established in numerous references notably Rodi (1982), Chen and Rodi (1980) and Schlichting (1979). In this study, the recorded scattered voltage and standard deviation profiles were compared with these well established concentration profiles.

## CHAPTER 3 THEORETICAL FRAMEWORK

### **Elastic and Inelastic Light Scattering**

There are two types of light scattering mechanisms: elastic scattering and inelastic scattering. In inelastic scattering there is a loss in energy of the incident wave and the scattered wave is emitted at a frequency different from the incident wave i.e  $h\nu_{\text{incident}} \neq h\nu_{\text{scattered}}$ . One of the types of inelastic light scattering is termed as Raman scattering and it involves a change in either the vibrational or rotational quantum number of the constituent molecule.

In elastic scattering of light, there is no loss of energy between the incident and the scattered wave. i.e  $h\nu_{\text{incident}} = h\nu_{\text{scattered}}$ . Elastic scattering is 2 to 3 orders of magnitude greater than inelastic scattering. This is the primary reason for choosing elastic scattering as a measurement technique since the signal strength is expected to be 2 to 3 orders of magnitude higher than the inelastic signal making it more easily discernible. The mechanism of elastic scattering is discussed in detail in below.

#### **Elastic Scattering Mechanism**

Consider an electromagnetic wave traveling through atmosphere. Scattering occurs whenever it encounters an obstacle in its path. This obstacle could be a gas molecule, dust particle or aerosols. For simplification, the term molecule is used in this description of the mechanism of elastic scattering. A molecule can be considered a mechanical oscillator carrying unequal masses and opposite charges at the center and periphery. The elastic scattering theory assumes that the molecules are non polar. This means that the

negative charge is uniformly distributed over the periphery and can be assumed to be at the center. Hence the electric dipole moment, which is the product of the charge and the separation distance, is zero in its stable state. In the presence of an electromagnetic wave the charges are forced apart due to the external electric field of the wave and an induced dipole moment is created. Since the field strength of the external electric field varies periodically, the induced dipole oscillates synchronously with the field. This oscillating dipole then emits a secondary wave at the same frequency as that of the primary wave. This secondary wave is the scattered wave.

### Mie Theory

Figure 3-1 shows the scattering geometry for Mie scattering.

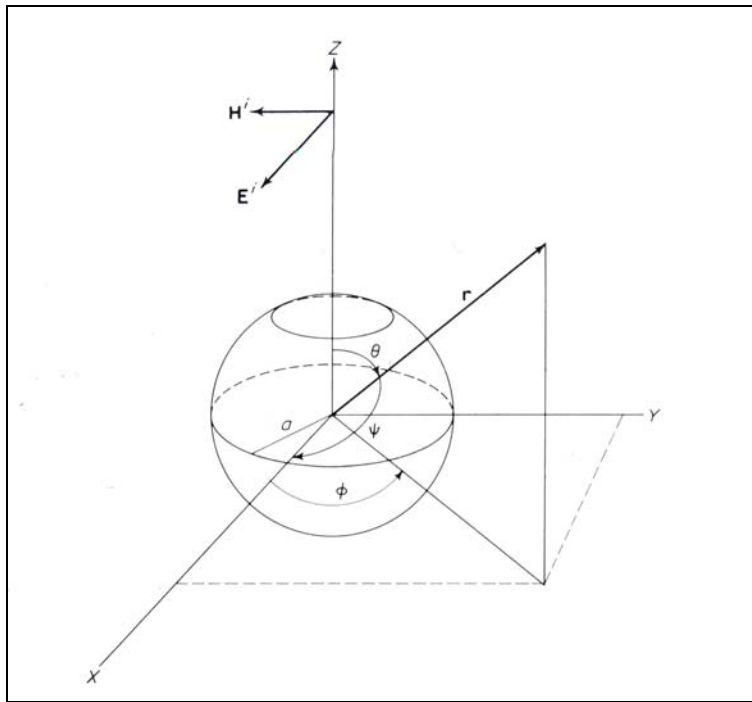


Figure 3-1. Mie scattering geometry.

The Mie theory describes the scattering of a plane electromagnetic wave by a particle of arbitrary size. The Mie theory originates from the exact solution of scattering of an electromagnetic wave equation (derived from the Maxwell relations) by a particle

and has been discussed in detail by Kerker (1969). A scattered wave is generated whenever a plane wave is incident upon a particle possessing a discrete boundary and a refractive index different from the surrounding medium.

In spherical co-ordinates the wave equation can be described as

$$\left[ \frac{1}{r^2} \frac{\partial r^2}{\partial r} \frac{\partial}{\partial r} + \frac{1}{r^2 \sin \theta} \frac{\partial \sin \theta}{\partial \theta} \frac{\partial}{\partial \theta} + \frac{1}{r^2 \sin^2 \theta} \frac{\partial^2}{\partial \varphi^2} + k^2 \right] \psi = 0 \quad (3.1)$$

The solutions to this equation are the Hertz- Debye potentials which can be obtained by the method of separation of variables as follows:

$$\psi = R(r)\Theta(\theta)\Phi(\varphi) \quad (3.2)$$

Each of these functions satisfies the following ordinary differential equations:

$$\frac{d^2 r R(r)}{dr^2} + [k^2 - \frac{n(n+1)}{r^2}] r R(r) = 0 \quad (3.3)$$

$$\frac{1}{\sin \theta} \frac{d}{d\theta} (\sin \theta \frac{d\Theta(\theta)}{d\theta}) + [n(n+1) - \frac{m^2}{\sin^2 \theta}] \Theta(\theta) = 0 \quad (3.4)$$

$$\frac{d^2 \Phi(\varphi)}{d\varphi^2} + m^2 \Phi(\varphi) = 0 \quad (3.5)$$

where n and m are integers.

The solutions of equation 3.3 are the Riccati Bessel functions defined as

$$\xi_n(kr) = (\pi kr/2)^{1/2} J_{n+1/2}(kr) \quad (3.6)$$

$$\zeta_n(kr) = -(\pi kr/2)^{1/2} N_{n+1/2}(kr)$$

where  $J_{n+1/2}(kr)$  and  $N_{n+1/2}(kr)$  are the half integer order Bessel and Neumann functions.

The solutions of equation 3.4 are the associated Legendre polynomials given by

$$\Theta = P_n^{(m)}(\cos \theta) \quad (3.7)$$

The solutions to 3.5 are the  $\sin(m\varphi)$  and  $\cos(m\varphi)$ .

The general solution of the scalar wave equation (3.1) (the Hertz –Debye potentials) can be obtained from a linear superposition of all of the particular solutions. The Hertz Debye potentials represent the solution for the incident wave, the scattered wave and the wave inside the particle. Only the Hertz Debye potentials for the scattered wave are discussed here. The Hertz Debye potentials for the scattered wave can be expressed in terms of an infinite series and are called the angular intensity distribution functions  $I_1$  and  $I_2$ .  $I_1$  and  $I_2$  are proportional to the perpendicular polarized and parallel polarized components of the light scattered at an angle  $\theta$  respectively.

$$I_1 = \left| \sum_{n=1}^{n=\infty} \frac{2n+1}{n+1} (a_n \pi_n(\cos\theta) + b_n \tau_n(\cos\theta)) \right|^2 \quad (3.8)$$

$$I_2 = \left| \sum_{n=1}^{n=\infty} \frac{2n+1}{n+1} (a_n \tau_n(\cos\theta) + b_n \pi_n(\cos\theta)) \right|^2 \quad (3.9)$$

$$\text{where } \pi_n(\cos\theta) = \frac{P_n^{(1)}(\cos\theta)}{\sin\theta} \quad (3.10)$$

$$\text{and } \tau_n(\cos\theta) = \frac{d}{d\theta} P_n^{(1)}(\cos\theta)$$

The constants  $a_n$  and  $b_n$  are obtained from the boundary conditions that the tangential components of the electric and magnetic field of the incident wave are continuous over the entire surface of the sphere. If the number density ( $N$ ) of the particle is known then the Mie scattering cross section for a single particle size can be defined as

$$\sigma_{\text{Mie}} = \frac{\lambda^2}{8\pi^2} N(I_1 + I_2) \quad (3.11)$$

The Mie scattering cross section is an indication of the intensity of light that would be scattered from a particle of arbitrary size.

### Calculation of intensity distribution functions $I_1$ and $I_2$

From equations (3.8) and (3.9) it can be seen that the intensity distribution functions  $I_1$  and  $I_2$  are in terms of complex infinite series and involve the calculation of the Legendre polynomials for every value of  $n$ . Also the constants  $a_n$  and  $b_n$  involve the calculation of Riccati Bessel functions for every value of  $n$ . As stated in Chapter 2, subroutines for the calculation of  $I_1$  and  $I_2$  are available. In this study one such program developed by the Oregon Medical Laser Center is used. The input parameters are the incident wavelength, particle size and refractive index. McCartney (1979) states that the refractive index of crystalline haze aerosols can be assumed to have a value of 1.33. The aerosols are assumed to be dielectric. This value is used throughout this study. It is to be noted that the angular intensity distribution functions depend on the refractive index and the value of 1.33 imposes a limiting condition since it does not take into account dry particles like soot. The values of  $I_1$  and  $I_2$  obtained from this subroutine are compared with published values of  $I_1$  and  $I_2$  in McCartney (1979). The comparison is done for five combinations of incident wavelength, refractive index and particle size. A typical comparison is shown in figures 3-2 and 3-3. Size parameter gives the relation between the size of the particle and the wavelength of incident light and is defined as

$$\alpha = \frac{2\pi a}{\lambda} \quad (3.12)$$

Figure 3-1 shows the values of  $I_1$  and  $I_2$  obtained as a function of scattering angle for a size parameter ( $\alpha$ ) of 0.5, (particle radius of 0.044 microns) and refractive index of sphere of 1.33. Using the program and figure 3-2 is obtained from McCartney for the same input parameters. The two figures are identical, establishing the accuracy of the subroutine.

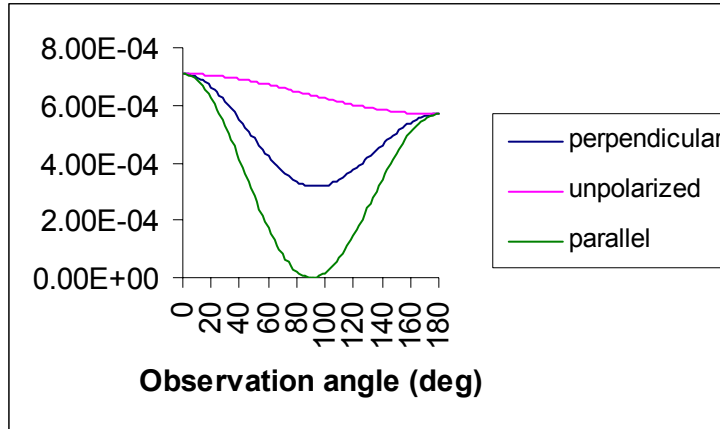


Figure 3-2.  $I_1$  (perpendicular) and  $I_2$  (parallel) intensity distribution functions for size parameter = 5, and refractive index = 1.33 obtained from the interactive webpage.

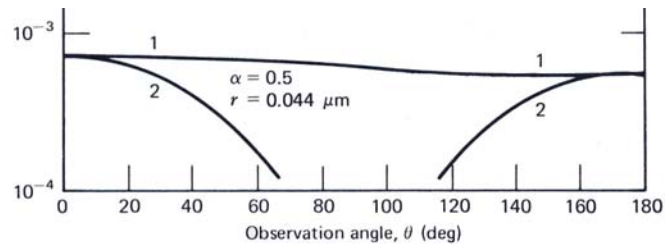


Figure 3-3.  $I_1$  (perpendicular) and  $I_2$  (parallel) intensity distribution functions for size parameter = 5, and refractive index = 1.33 from McCartney.

### Rayleigh Theory

The Mie solution is a complex mathematical solution. For particles of size much less than the wavelength of incident light, the Mie series solution converges in one term and is called the Rayleigh theory. The Rayleigh theory was originally put forth by Lord Rayleigh (J.W. Strutt, third Baron of Rayleigh) in 1871, long before the Mie solution was developed (1908). Later on it was proved that the Rayleigh theory is actually a single term simplification of the Mie theory. Lord Rayleigh put forth the Rayleigh theory principally to explain the blue color of the sky. He assumed that the particles were

spherical, isotropic, much smaller than the wavelength of incident light and denser than the surrounding medium. Through straightforward dimensional reasoning he arrived at the conclusion that scattering varies directly with the square of the particle volume and inversely as the fourth power of the wavelength of incident light.

The scattering by gas molecules is in the Rayleigh regime because of the small size of the molecules. McCartney (1976) gives a good physical description of Rayleigh scattering. He states that for the Rayleigh theory to be applicable,  $\alpha \ll 1$  or the particle radius should be at least 0.03 times less than the wavelength of incident light. The following are the assumptions about the molecules for Rayleigh scattering.

1. The molecules are non ionized implying that there is no overall charge over the entire molecule. This means that the molecule does not experience a net force in an electric field.
2. The molecules are non polar meaning that the electronic charge is uniformly distributed over the shell and could be treated to be at the center. Even though the polar assumption is made in the original theory, the Rayleigh theory is valid for non-polar particles as well.
3. The molecule is isotropic implying that the forces experienced within the molecule are balanced.
4. The molecule is linear which means that the binding forces within the molecule obey Hooke's law.
5. The molecules are lightly damped meaning that the amplitude of oscillation does not become too large at frequencies near resonance.

These assumptions are applicable to ordinary gas molecules like nitrogen and helium.

Based on these assumptions McCartney (1976) derives the differential Rayleigh scattering cross section for perpendicular polarized scattered light as

$$\sigma_{\text{Rayleigh}} = \frac{128\pi^5 a^6}{3\lambda^4} \left| \frac{n^2 - 1}{n^2 + 2} \right| \quad (3.13)$$

As seen from equation (3.13) the Rayleigh scattering cross section is independent of the scattering angle and has an inverse fourth power dependence on the wavelength of incident light. It also depends on the refractive index ( $n$ ) of the particle.

### Photon arrival rate calculations for Rayleigh and Mie theory

Knowing the Rayleigh and Mie scattering cross sections the intensity of scattered light can be calculated for a given set of experimental constants. Both the Rayleigh and Mie scattering cross sections are applicable for an individual molecule and are not functions of the gas number density  $N$  assuming independent scattering. For a given volume of a gas the intensity of scattered light is linearly proportional to the gas number density. The scattering from multiple molecules in a given volume can be considered to be additive, independent and incoherent because of the random spacing and thermal motion of the gas molecules.

Thus for an incident beam of energy  $I_0$ , scattered from a control volume with molecular number density  $N$ , the intensity of the scattered beam is proportional to the scattering cross section of the molecule, the number density and the energy of incident beam

$$I_{\text{scat}} = C(I_0\sigma N) \quad (3.14)$$

The proportionality constant  $C$  is defined by the scattering geometry, namely the solid angle of the collection optics ( $\Omega$ ), control volume ( $dV$ ) and optical efficiency of the collection optics ( $\eta$ ). In this study, the scattered beam was collected using a 60 mm diameter lens at a distance of 250 mm from the scattering volume which define the solid angle. The control volume depends on the angle at which the scattered beam is collected and is discussed in chapter 4. The optical efficiency was assumed to be 90% for each optical surface the scattered beam is passed through. Thus for Rayleigh scattering the intensity of scattered light from a control volume containing a mixture of gases is given by

$$I_{\text{Rayleigh}} = (I_0)(\eta)(dV)(\Omega)\Sigma(N\sigma_{\text{Rayleigh}})_i \quad (3.15)$$

And scattered intensity for Mie scattering is given by

$$I_{\text{Mie}} = (I_o)(\eta)(dV)(\Omega)\Sigma(N\sigma_{\text{Mie}})_i \quad (3.16)$$

Knowing the Rayleigh and Mie scattered intensities, the total scattered intensity received at the collection lens can be calculated as

$$I_{\text{total}} = I_{\text{Rayleigh}} + I_{\text{Mie}} \quad (3.17)$$

### Scattering Cross Section Considerations

In this study, pure helium and a mixture of 20% helium and 80% nitrogen are used. The scattering cross section of helium is 0.015 times the scattering cross section of air and the scattering cross section of pure hydrogen is 0.23 times the scattering cross section of air. In order to match the scattering cross section of hydrogen, a mixture of 20% helium and 80% nitrogen is used. The differential scattering cross sections of hydrogen, helium and nitrogen are listed at a wavelength of 532 nm in table 3-1.

Table 3-1. Scattering cross section at a wavelength of 532 nm.

Gas	Scattering Cross Section ( $\sigma$ ) ( $\text{m}^2/\text{sr}$ )
Air (Nitrogen)	8.16E-32
Hydrogen	1.88E-32
Helium	1.22E-33

Knowing these values, the mixture concentration of 20% helium and 80% nitrogen are obtained using the following relation ( $x = \% \text{ helium}$ )

$$\sigma_{\text{hydrogen}} = x \sigma_{\text{helium}} + (1-x) \sigma_{\text{nitrogen}}. \quad (3.18)$$

### Buoyant Jet Theory

Buoyancy forces arise in a jet if the density of the flow fluid is different from the density of the surrounding fluid. In the absence of buoyancy forces the jet is called a non buoyant jet. In the other limiting case when the buoyancy force dominates the flow, the

jet is called a plume. Thus the non buoyant jet has about the same density as the surrounding environment so that the buoyancy forces are absent, whereas a pure plume has no initial momentum. The densities of both flow fluids used for the experiments- pure helium and the mixture of helium and nitrogen are different from the density of the surrounding fluid (ambient air). The Froude number is used to characterize whether a jet is a non buoyant jet, a buoyant jet or a plume-Chen and Rodi (1980). The Froude number is the ratio of inertial forces to buoyancy forces and is defined as

$$Fr = Re/Gr^2 \quad (3.19)$$

Reynolds number is the ratio of the inertial forces to the viscous forces and can be written as

$$Re = \frac{\rho v d}{\mu} \quad (3.20)$$

The Grashof number (G) is defined as

$$\frac{g(\rho_a - \rho_o)D^3}{\rho_o \nu} \quad (3.21)$$

And it is the ratio of buoyant to viscous forces.

In a non buoyant jet, only the Reynolds number is of influence ( $Fr=\infty$ ) whereas in pure plumes only the Grashof number is dominant ( $Fr=0$ ). For an axisymmetric vertical jet, the limiting condition for a buoyant jet is defined in Chen and Rodi as follows

$$0.5 < Fr^{-1/2} (\rho_o/\rho_a)^{-1/4} (z/D) < 5 \quad (3.22)$$

### **Froude Number Calculation**

Two different nozzle diameters of 1/4" and 1/2" are used. Also two flow fluids (pure helium and mixture of 20% helium and 80% nitrogen) are used. Four different cases are considered: 1/2" diameter nozzle with pure helium, 1/2" diameter nozzle with a mixture of 20% helium and 80% nitrogen, 1/4" diameter nozzle with pure helium and 1/4" diameter

nozzle for a mixture of 20% helium and 80% nitrogen. The measurements are taken for four downstream distances of 2, 4, 6, and 8 nozzle diameters. The Reynolds number is chosen as 500 for each case.

The criterion for buoyant jet (equation 3.21) is tested for all four combinations of nozzle diameters and flow fluid and at all four downstream distances. Table 3-2 lists the values of Froude numbers for all four combinations of nozzle diameters and flow fluid and for the two limiting cases of 2 and 8 nozzle diameters downstream.

Table 3-2. Froude number calculations show that the criteria for buoyant jet is met for all combinations of flow fluids, nozzle diameters and downstream distances

Cases	Reynolds Number(Re)	Froude Number(Fr)	$0.5 < Fr^{-1/2}(\rho_o/\rho_a)^{-1/4}z/D < 5$	
			2 nozzle diameters	8 nozzle diameters
1. ½ "; He	500	36.5	0.521	2.08
2. ½ "; 20%He, 80%N2	500	64.5	0.54	2.16
3. ¼ "; He	500	292.5	0.88	3.52
4. ¼ "; 20%He, 80%N2	500	516.5	0.94	3.76

### Buoyant Jet Profiles and Concentration Variation

Figure 3-4 shows the instantaneous and time averaged profiles of a buoyant jet. The jet centerline is characterized by a potential core near the nozzle exit. Inside the potential core, the concentration of the flow fluid is 100%. The shear layers define the jet spread angle ( $\beta$ ). The edge of the shear layers mark the boundary of the time averaged profile. The concentration of the flow fluid varies from a 100% at the jet centerline to 0% at the edge of the shear layers. Chen and Rodi (1980) have listed the spread angles of non- isothermal jets. In this study a spread angle of  $13^\circ$  is found for a vertical round buoyant jet.

Chen and Rodi (1980) summarize empirical data predicting the axial spread of an axisymmetric vertical buoyant jet. The concentration at any point in the shear layer of a buoyant jet can be calculated using the following relation.

$$\frac{C - C_a}{C_{cl} - C_a} = \exp [-K_c(r/z)^2] \quad (3.23)$$

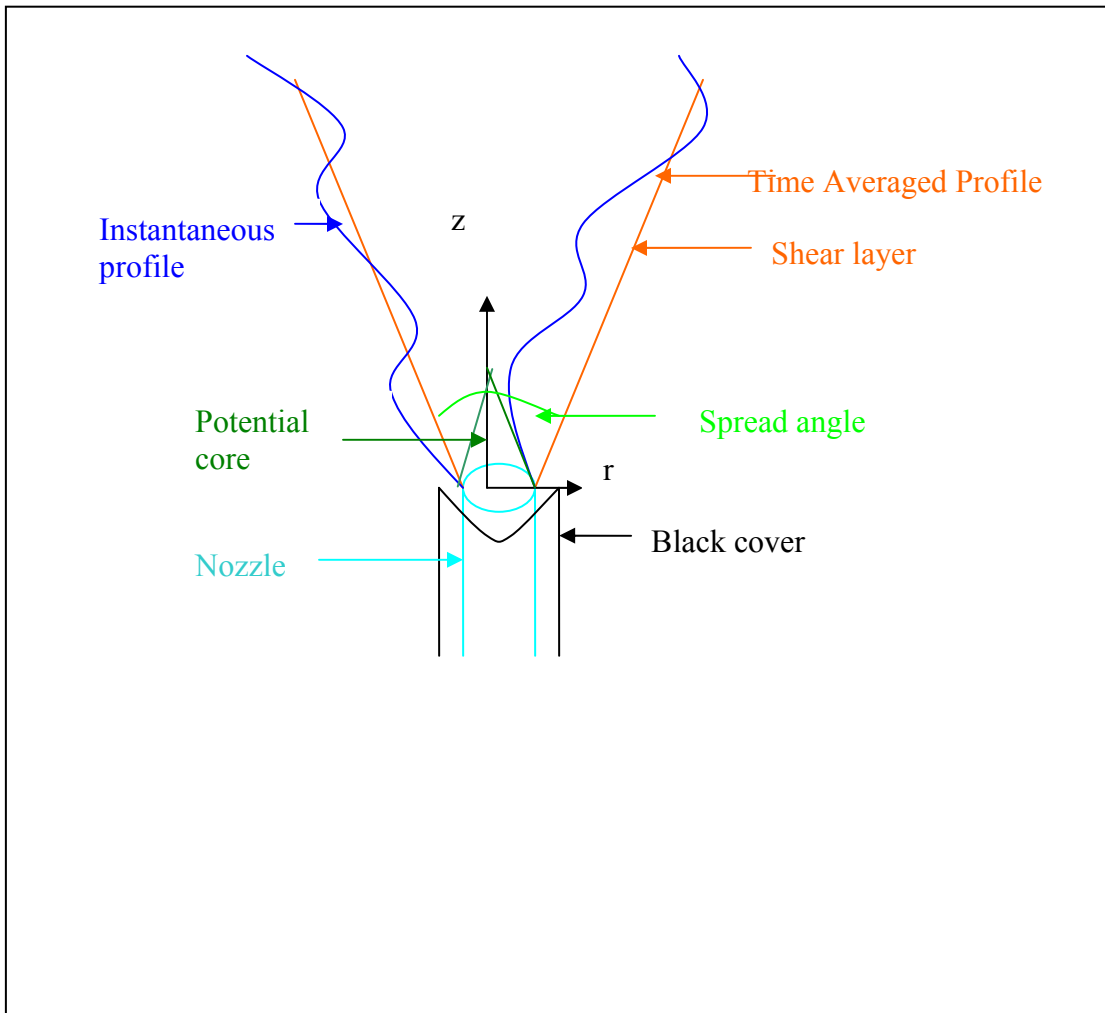


Figure 3-4. Instantaneous and time averaged profiles of a typical buoyant jet.

The constant  $K_c$  is related to the jet spread angle  $\beta$  as

$$K_c = \ln 2 / (\tan\beta/2)^2 \quad (3.24)$$

So, for a jet spread angle of  $13^\circ$ ,  $K_c = 53.4$

For a vertical buoyant jet, the centerline concentration ( $C_{cl}$ ) is found from the dimensionless density ( $C^*$ ) using the following equation

$$\frac{C_o - C_a}{C_{cl} - C_a} = C^* = 4.4Fr^{1/8}(\rho_o/\rho_a)^{-7/16} (z/D)^{-5/4} \quad (3.25)$$

Using this value of  $Kc$  the concentration of the flow fluid at any point in the flow can be calculated using equation 3.22.

For both the  $\frac{1}{2}$ " diameter nozzle and the  $\frac{1}{4}$ " diameter nozzle,  $C - C_a / C_{cl} - C_a$  is plotted as a function of radial distance ( $r$ ) for a downstream distance ( $z$ ) of 2 nozzle diameters for each case as seen in figure 3-5.

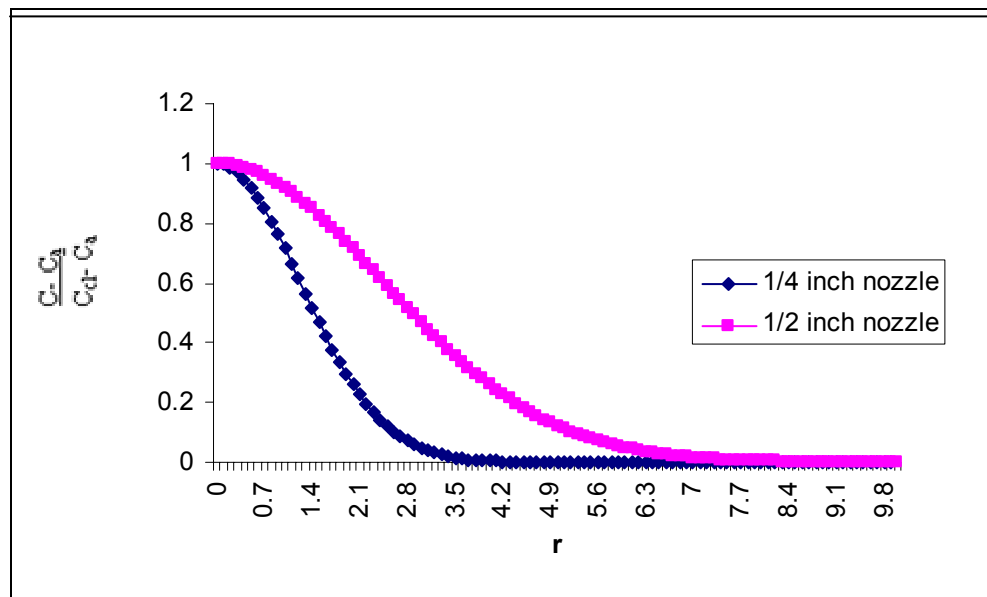


Figure 3-5. Concentration variation with  $r$  for  $z = 2$  is Gaussian in nature for both nozzle diameters of  $\frac{1}{4}$ " and  $\frac{1}{2}$ ".

## CHAPTER 4 EXPERIMENTAL SCHEME

### **Collection at 90° and Backscatter**

The goal of the project is to detect the change in intensity of scattered light in the presence of hydrogen. Rayleigh scattering is independent of the angle at which the scattered light is collected but the Mie signal depends on the scattering angle. Initially, the collection optics were set at 90° to the incident beam and the measurements were focused on a single point of the beam as seen in figure 4-1. An advantage of this optical configuration is that the glare from the incident beam on the scattered signal is minimum at this angle since the minimum incident beam area is visible to the photomultiplier tube.

For field measurements since the exact position of the leak could be at any distance from the laser, the drawback with a 90° scattering scheme would be that the collection optics consisting of the collecting, focusing lenses, filter, photomultiplier tube and the digital oscilloscope would have to be moved depending on the position of the suspected leak. It would be ideal to use a scheme in which the collection optics could be kept stationary. This can be done by using a backscatter scheme in which the incident light is passed between two 4" (101.6mm) square mirrors and the scattered light is collected at a 180° using the two mirrors. The mirrors are 90% reflective at a wavelength of 532 nm. The backscatter scheme is shown in figure 4-2. For the backscatter scheme, since the angle of observation is a 180°, the control volume is defined by the beam area and the pulse width of 5 ns (1.5m). This leads to a fall in the signal to noise ratio as the leak occupies only 0.6% of the control volume as discussed in Chapter 5.

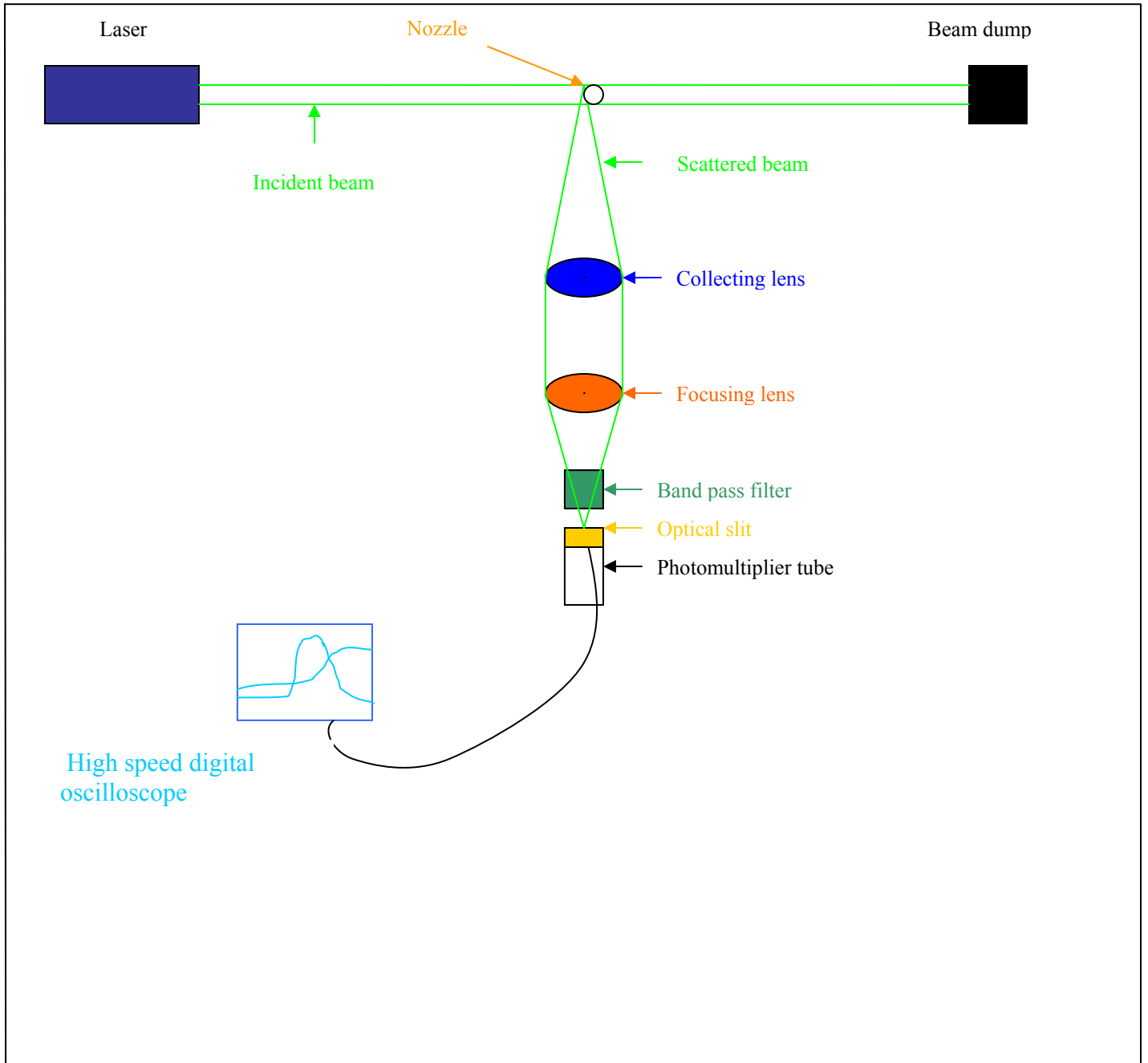


Figure 4-1. Experimental scheme for collection of scattered light at 90°

The back scattering scheme uses the same set of collection optics as that for the 90° scattering scheme except that the 90° scheme uses a 60 mm collecting lens. From ray tracing it is found that the beam divergence angle of the scattered beam arriving at the

mirrors was  $0.4^\circ$  and so the scattered rays reflected from the mirrors are effectively collimated and could be focused on the photomultiplier tube.

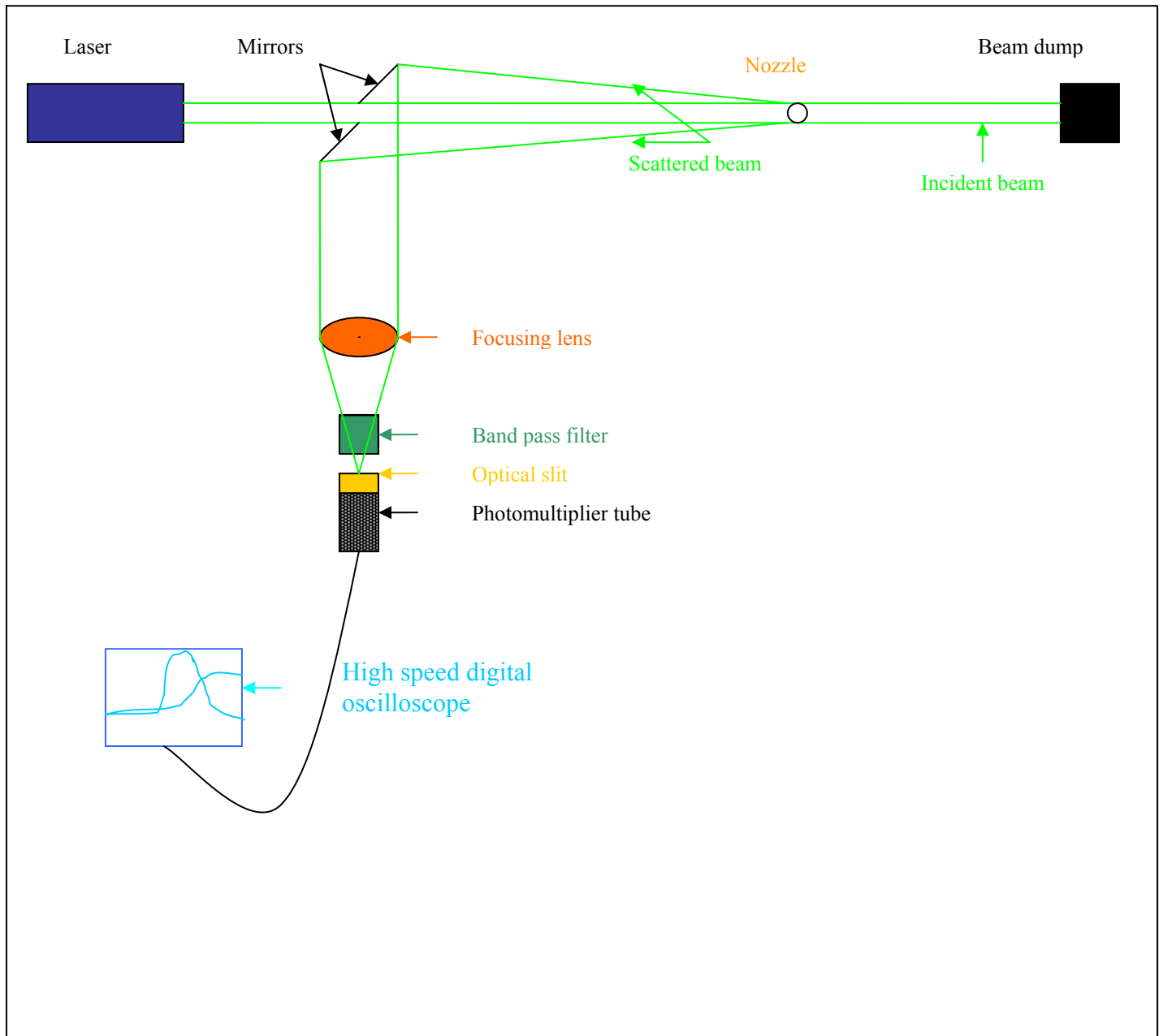


Figure 4-2. Experimental scheme for collection of scattered light at a  $180^\circ$  (back scatter)

The following components constitute the optical set up shown in figures 4.1 and

4.2.

**Laser.** Initially the experimentation was done using an argon ion laser operated on the 488 nm wavelength. The laser power was set at 3 W and the beam diameter was 1mm with a beam divergence angle of  $0.06^\circ$ . The argon ion laser is a continuous beam low power laser. In order to amplify the scattered signal and for higher temporal resolution a pulsed Nd:YAG laser was also used. The laser power is 200 mJ/pulse at a wavelength of 532 nm. The pulse width was 5 nanoseconds and the frequency is 10 Hz. The beam diameter is 6 mm with a beam divergence angle of  $1.1^\circ$ . Since the beam diameter was larger than the Argon-Ion laser, the Nd:YAG laser defined a larger control volume than the Argon-Ion laser. Thus two different power lasers at two wavelengths are used for the experiments.

**Nozzle.** The leak was simulated using a nozzle. The laser beam was passed directly over the nozzle. The nozzle is placed at a distance of 8 feet (20.32 cm) from the laser for the  $90^\circ$  scattering scheme. Using the beam divergence angle, the beam diameter over the nozzle was calculated to be 1.1 mm for the Argon ion laser and 8 mm for the pulsed Nd:YAG laser. In order to analyze the effect of the relative size of the beam and leak, two different nozzle diameters are used. For initial measurements using the argon ion laser a  $\frac{1}{2}$ " (12.6mm) nozzle was used. For the pulsed laser a  $\frac{1}{4}$ " (6.3mm) diameter nozzle was used. Thus for the argon ion laser, the beam diameter is 11.5 times less than the leak diameter whereas for the Nd:YAG laser the beam diameter is 1.25 times more than the leak diameter. The back scattering scheme uses the pulsed Nd:YAG laser with the  $\frac{1}{4}$  diameter nozzle. The nozzle is placed at a distance of 20 feet (50.8 cm) from the laser and the beam diameter is 10 mm over the nozzle. The Reynolds number of the leak is set at 500 for both nozzle diameters and the Froude number was calculated as

discussed in chapter 3 and presented in table 3.1. This combination of Reynolds and Froude number ensured that the leak is a buoyant jet. The nozzle is covered with a black felt drape to minimize glare. The mass flow rate of pure helium and the mixture of helium and nitrogen is monitored using mass flow controllers.

**Nozzle mounting.** Three micrometer traverses are used for mounting the nozzle for three dimensional motion. Each traverse has a least count of 0.05 mm. Figure 4-3 shows the schematic of the mounting used. This allowed the measurements to be taken at different downstream locations.

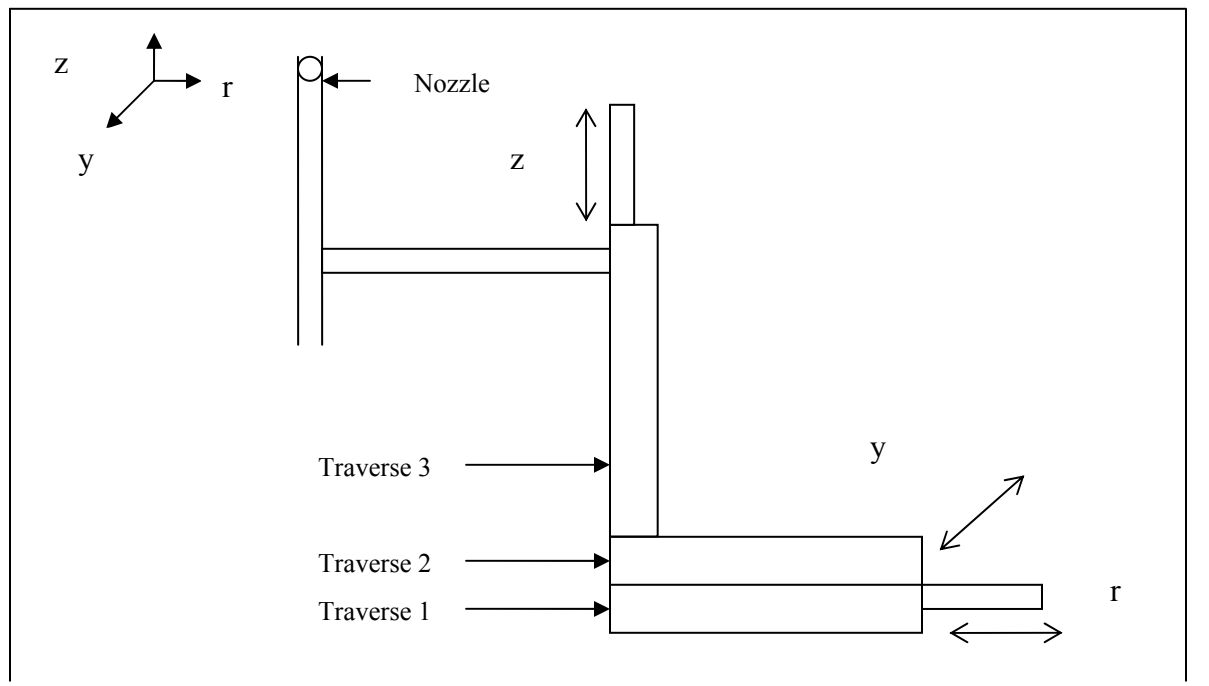


Figure 4-3. Nozzle mounting showing three dimensional motion capability.

**Beam dump.** The incident laser beam was trapped using a beam dump. The beam dump was placed at a distance of 20 feet from the nozzle to minimize glare.

**Collection optics.** The scattered beam was collected using a set of collection optics which consisted of a collecting lens, focusing lens, band pass filter and a

photomultiplier tube. The collection optics were covered with a black felt drape in order to eliminate additional glare.

**Collecting lens.** The collecting lens is a 60 mm diameter lens and has a focal length of 250 mm. As seen from figure 4-1 the focal point of the lens coincides with the nozzle position so that scattered light collected by the lens is collimated. As seen from figure 4-2 the collection lens was not used for the backscattering geometry because the scattered beam reflected from the two mirrors was collimated.

**Focusing lens.** The focusing lens is a 60 mm diameter lens and had a focal length of 124 mm. The collimated beam from the collecting lens is focused on the Photomultiplier tube using the focusing lens.

**Band pass filter.** For the Nd:YAG laser, the band pass filter is a 532 nm line filter that blocks background light at other wavelengths from reaching the photomultiplier tube. The band pass filter was kept at a distance of 3 mm from the Photomultiplier tube.

**Photomultiplier tube.** The scattered beam is focused on the Photomultiplier tube. The Photomultiplier tube is a Hamamatsu model number HC 120-01 tube and has a built in amplifier with adjustable gain. It has a rise time of 2 ns and a bandwidth of 23 Khz. This means that the photomultiplier tube can distinguish between two signals that are 44 microseconds apart. Since the frequency of the pulse laser is 10 Hz the interval between two consecutive pulses is almost 1ms. Hence for a 90° scattering geometry, the photomultiplier tube can distinguish between two consecutive pulses. From the manufacturer's specifications the calibration constant of the photomultiplier is found to be 121 V/nW which allows the conversion of the voltage recorded on the photomultiplier tube into power. The Photomultiplier tube has a 0.015 mm optical slit mounted on it to

minimize the intensity of scattered light. The Photomultiplier tube converts the photonic signal to electrical voltage which is then sent to a high speed digital oscilloscope. It is important to note that even though the photomultipliers are considered to be highly linear devices, the linearity generally occurs over a lesser range for the pulsed Nd:YAG laser. ( $\lambda = 532 \text{ nm}$ ) at varying flash lamp discharge voltage. Figure 4-4 displays the photomultiplier tube voltage as a function of varying flash lamp discharge voltage.

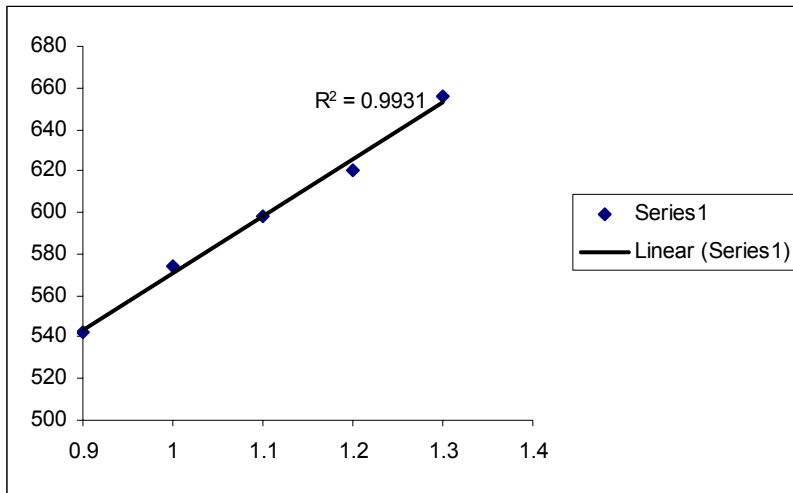


Figure 4-3. Photomultiplier tube linearity tested as a function of flash lamp voltage

**High Speed Digital Oscilloscope.** The photomultiplier tube signal is recorded on a high speed digital oscilloscope (LeCroy). It has two channel simultaneous data acquisition capabilities. It is triggered externally using the pulsed laser. The trigger time is 180 ns which means that the laser sends an electric signal to the oscilloscope exactly 180 ns before it fires the pulse so that the oscilloscope can be set to capture the scattered signal. The oscilloscope acquires data over a time period of 50 microseconds. The measurements are recorded and readout on a spreadsheet.

**Control Volume.** For the  $90^\circ$  scheme, the control volume is defined by the beam diameter and the length of the control volume is defined by the width of the optical slit

(150 microns).

### **Back Scatter Considerations**

As previously stated the back scattering scheme is used to test the feasibility of the technique for field measurements. An important consideration for field measurements is the ability to detect the leak over longer distances. Hence the leak is created by placing the nozzle at a distance of 20 feet (50.8 cm) the laser beam. The beam dump is placed at a distance of 10 feet (25.4 cm) from the nozzle. The control volume is defined by the beam diameter and the length of the control volume for this case is defined by the pulse width (5nanoseconds =1.5m)

### **Data Recording Procedure**

The measurements were done at four different downstream locations of 2, 4, 6 and 8 nozzle diameters for the pulsed Nd:YAG laser and two downstream locations of 2 and 6 nozzle diameters for the argon ion laser. For each downstream distance the nozzle was traversed along the direction of the beam using the micrometer traverse as shown in figure 4-3. The steps in which the nozzle was traversed was calculated from the spread angle of the jet as seen in figure 4-4. The distances 1a, 2b, 3c and 4d varied depending on the nozzle diameters ( $\frac{1}{4}$ " or  $\frac{1}{2}$ "). This was done so that the measurements done at all four downstream distances could be graphed on the same scale of  $r/z$ .

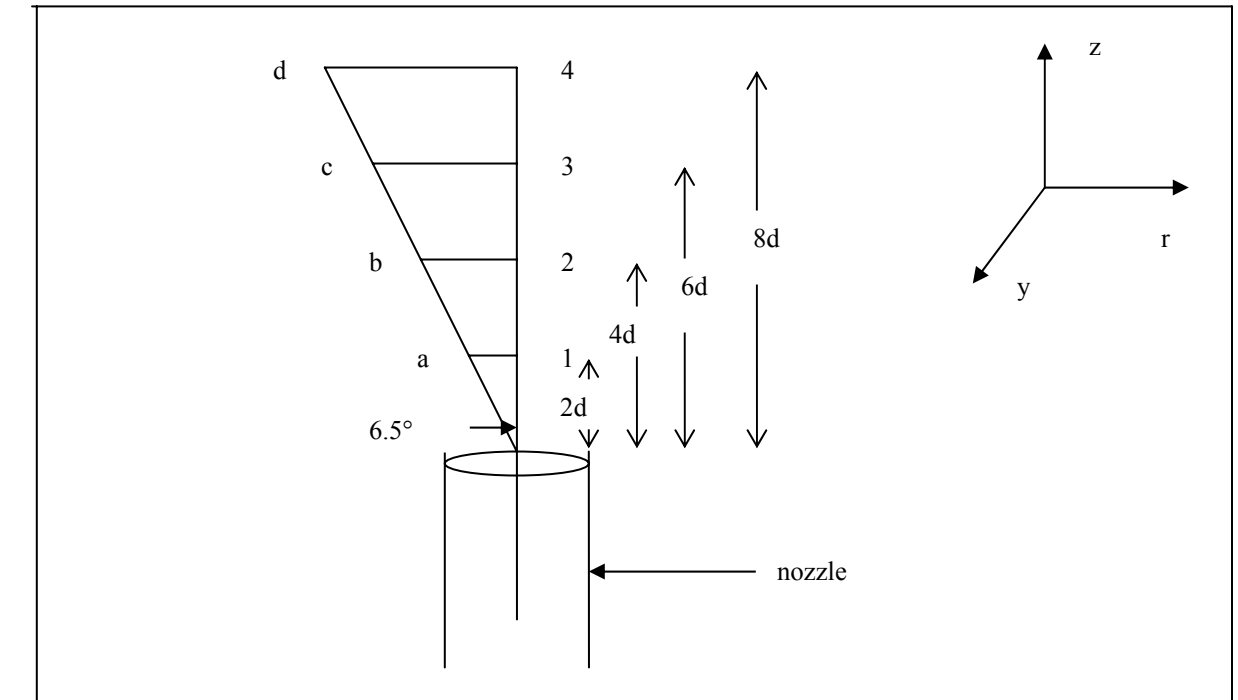


Figure 4-4. Calculation of nozzle traverse distances for downstream distances of 2, 4, 6 and 8 nozzle diameters using jet spread angle of  $13^\circ$ .

CHAPTER 5  
RESULTS AND DISCUSSION

**Comparison of Theoretical and Experimental Photon Arrival Rate**

This section discusses how the theoretical and experimental photon arrival rates compare. In chapter 3 the equations for calculating the Rayleigh photon arrival rate (equation 3.15) and Mie photon arrival rate (equation 3.16) are presented. The total theoretical photon arrival rate is calculated as a sum of the Rayleigh and Mie photon arrival rates (equation 3.17).

**Calculation of Theoretical Rayleigh Photon Arrival Rate.**

In the presence of helium, the Rayleigh photon arrival rate can be calculated by modifying equation 3.15 as follows. The percent helium (x) was varied from 0 to 100 and the resulting photon arrival rate is shown in figure 5.1.

$$I_{\text{Rayleigh}} = (I_0)(\eta)(dV)(\Omega)N(x\sigma_{\text{He}} + (1-x)\sigma_{\text{air}}) \quad (5.1)$$

$$I_0 = 7.07\text{E}+6 \text{mj/m}^2\text{-pulse} = 1.88\text{E}22 \text{ photons/ m}^2\text{-pulse(Nd:YAG laser) ;}$$

$$3.8\text{E}+6 \text{ W/ m}^2 \text{ (Argon-Ion laser)}$$

$$\eta = (0.9)^5$$

$$dV = 1.2 \text{ E-}8\text{m}^3 \text{ (90}^\circ \text{ scatter); } 1.2\text{E-}4\text{m}^3 \text{ (backscatter)}$$

$$\Omega = \pi(60)^2/(250)^2 \text{ sr (90}^\circ \text{ scatter); } (2)(101.6)^2/(12100)^2 \text{ sr (backscatter)}$$

$$N = 2.2\text{E}25 \text{ molecules/m}^3$$

$$\sigma_{\text{He}} = 1.22\text{E-}33 \text{ m}^2/\text{sr}$$

$$\sigma_{\text{air}} = 8.16\text{E-}32 \text{ m}^2/\text{sr}$$

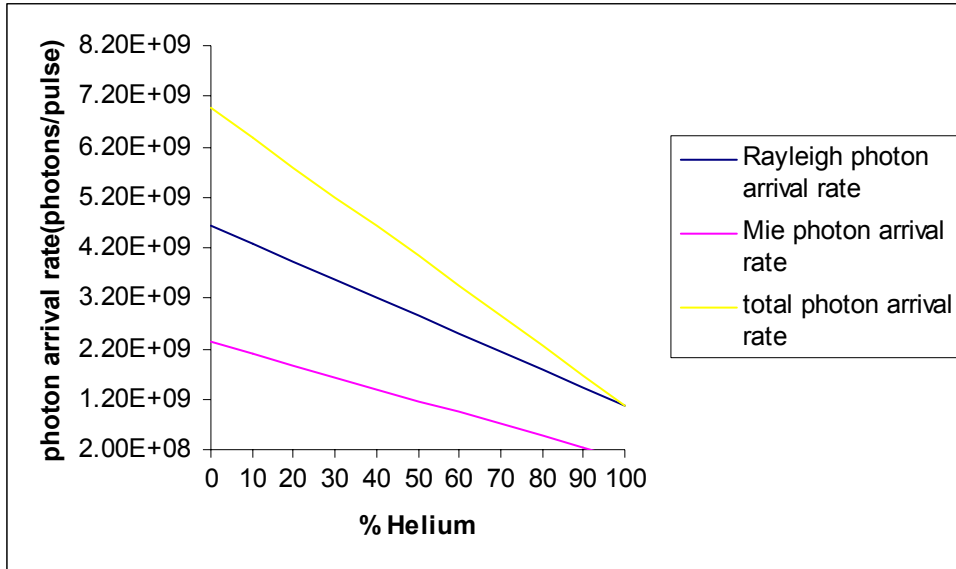


Figure 5-1. Theoretical photon arrival rate calculations show that Rayleigh signal is higher than Mie signal.

### Calculation of Theoretical Mie Photon Arrival Rate

Equation 3.16 is used for the calculation of the Mie photon arrival rate.

$$I_{\text{Mie}} = I_0(\eta)(dV)(\Omega)\Sigma(N\sigma_{\text{Mie}})_i \quad (3.16)$$

The two unknowns in this equation are  $N_i$  and  $(\sigma_{\text{Mie}})_i$

The calculation of  $(\sigma_{\text{Mie}})_i$  involves the use of the intensity distribution functions  $I_1$  and  $I_2$ . If the particle size is known, these functions can be calculated for a given wavelength of incident light using the subroutine as discussed in Chapter 3. Two size distributions were used to determine the size of particles in the ambient air and also the number density of particles of a particular size.

Distribution 1 uses the data from a LASAIR II particle counter. Table 5-1 shows a typical output of the particle counter data.

The sampling is done in the laboratory for a sampling time of 1 minute and the volume of particles sampled over this period is 1 cubic feet. The particle size is given in column 1. Columns 2 and 3 give the lower and upper limits of the number of particles of

the corresponding size. An average of columns 2 and 3 is taken. Thus using the LASAIR II data, the number density-particles per m<sup>3</sup> ( $N_i$ ) of a particular size are known. For each particle of size of 0.3, 0.5, 1, 5, 10, 25 microns the Mie scattering subroutines are used to calculate  $I_1$  and  $I_2$  at a wavelength of 532 nm for the pulsed Nd:YAG laser. Knowing  $I_1$  and  $I_2$ ,  $\sigma_{Mie}$  is calculated using equation 3.11 and the Mie scattered intensity using equation 3.16. To account for the presence of helium equation 3.16 was modified as

$$I_{Mie} = I_0 \eta l \Omega N \sigma_{Mie} (1 - x_{He}) \quad (5.2)$$

Table 5-1. Particle counter data show the particle distribution in the lab.

Particle size (microns)	Number of particles/ft <sup>3</sup> (lower limit)	Number of particles/ft <sup>3</sup> (upper limit)
0.3	25268	27272
0.5	7864	9222
1	1164	1298
5	100	104
10	12	12
25	1	1

For distribution 2 the typical maritime aerosol distribution in McCartney (1969) is used. Figure 5-2 shows particle distribution for stratospheric dust particles or hailstones (model H), continental aerosols (model L) and maritime aerosols (model M). The maritime aerosol distribution (model M) is chosen since it is appropriate for Cape Canaveral.

The number density per radius interval  $n(r)$  for this distribution is calculated using the following fit (McCartney)

$$n(r) = ar^\alpha \exp(-br^\gamma) \quad (5.3)$$

Where the constants  $a$ ,  $b$ ,  $\alpha$ ,  $\gamma$  have the following empirically determined values

$$a = 5333$$

$$b = 8.9443$$

$$\alpha = 1$$

$$\gamma = 1/2.$$

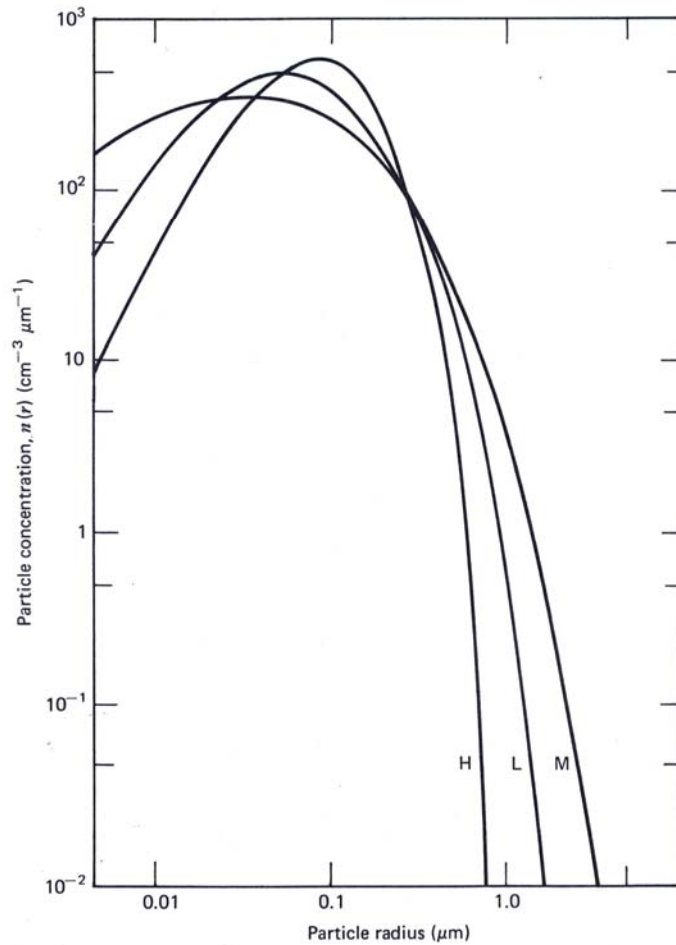


Figure 5-2. Model M shows maritime distribution of aerosols which is used to calculate the particle size distribution.(McCartney 1979, page 139)

Using the values of particle size ( $r$ ) ranging from 0 to 25 microns, and the above values of the constants, the model M (log-log scale) was duplicated on a regular scale as shown in figure 5-3.

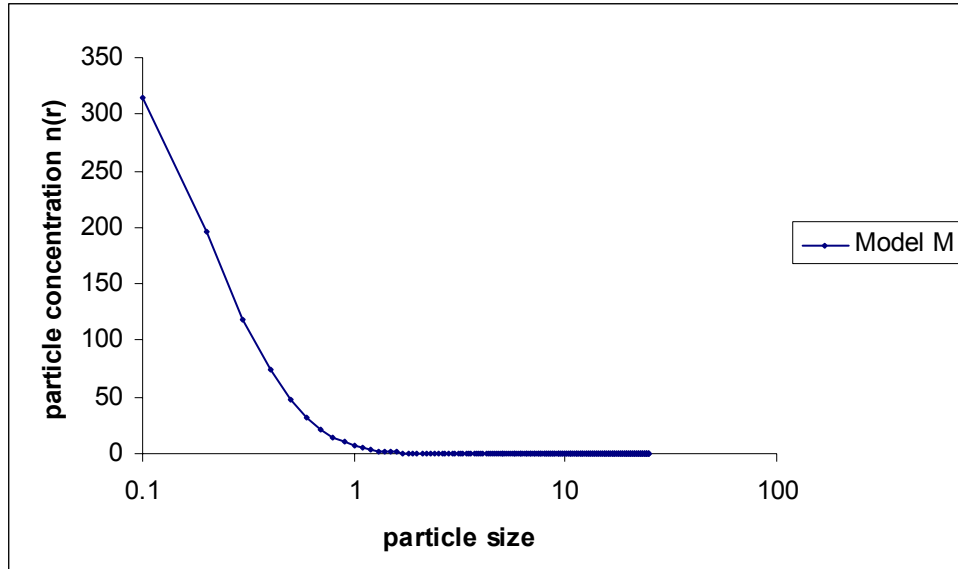


Figure 5-3. Model M duplicated for calculating the number density using radius interval on a log-normal scale.

The number density is calculated for the same particle radii as the LASAIR II data. ( $i = 0.3, 0.5, 1, 5, 10$  and  $25$  microns) by integrating the area under the curve shown in figure 5-2 using following equation. The interval ( $i$ ) to ( $i+1$ ) represents the difference between the two consecutive particle radii

$$N_i = \sum_{i=1}^{i=6} 0.5(n(r)_i + n(r)_{i+1})I \quad (5.4)$$

The values of number density  $-N_i$  (particles/ $m^3$ ) obtained from equation are compared with the values of  $N_i$  from the particle counter (Table 5.1). Figure 5-4 shows this comparison. As seen from the figure the particle distribution for maritime and lab aerosols is similar.

For distribution 2 since the number density and the particle radius are known (equation 5.4) the Mie scattering cross section and the intensity of Mie scattered signal is calculated using the same approach as in distribution 1.

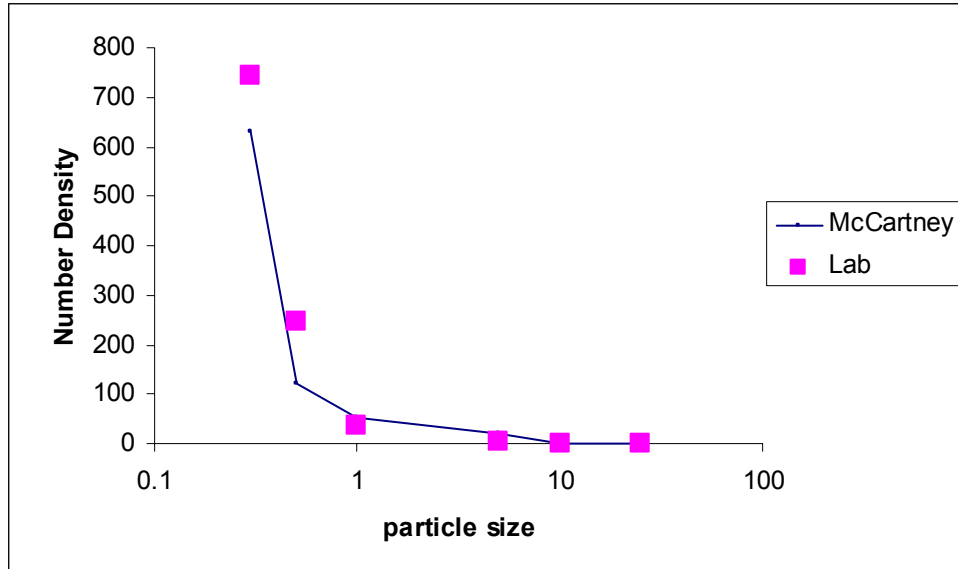


Figure. 5-4. Comparison of number density of maritime and lab aerosols shows similarity

Figure 5-5 shows the comparison between the Mie photon arrival rates for the two distributions. The value of  $I_0$  used is that for the pulsed Nd:YAG laser.

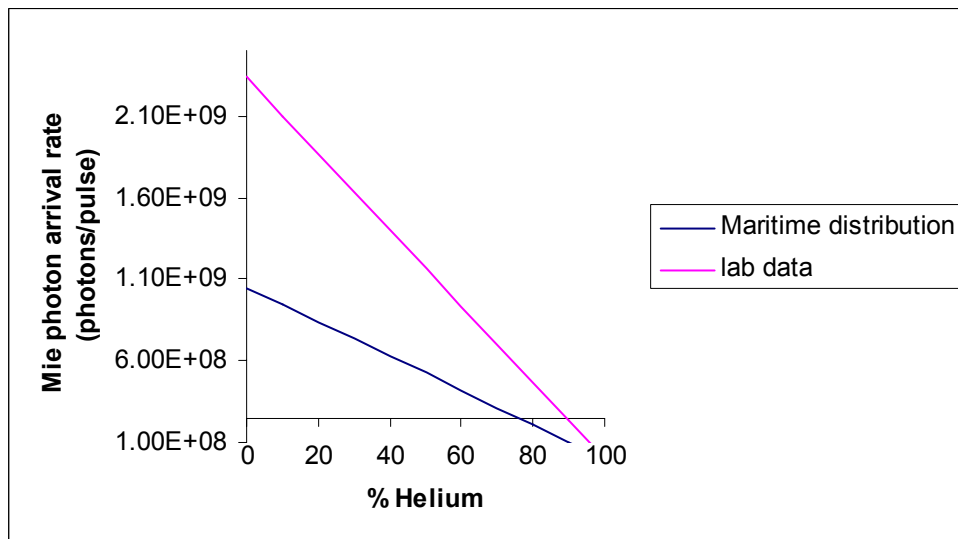


Figure 5-5. Effect of maritime and lab aerosol distribution on Mie scattered intensity shows that both signals are of the same order of magnitude.

As seen from the graph, both signals are of the same order of magnitude. The maximum difference between the two signals (55%) is for the case of 0% helium since all

Mie scattering particles have been displaced, and no ambient air is in the control volume. Both signals tend to zero as the helium concentration approaches 100%. This figure shows that the Mie signal would be of the same order and smaller for maritime field measurements as that for laboratory measurements.

### **Calculation of Total Theoretical Photon Arrival Rate**

For the calculation of  $I_{Mie}$  the data from the particle counter is used since it represents aerosol distribution for the experimental conditions. Knowing  $I_{Rayleigh}$  and  $I_{Mie}$ , the total theoretical photon arrival rate is calculated using equation 3.17. Figure 5-1 shows the variation of Rayleigh, Mie and total photon arrival rate with percent helium. The value of  $I_0$  used here is for the pulsed Nd:YAG laser.

An important result of the theoretical study is that the Mie scattered signal is lesser than the Rayleigh scattered signal. Initially it was reasoned that the Mie scatters would augment the scattered signal since in the presence of helium the total signal would fall due to reduction in Mie signal. This study shows that although this factor is present it influences the total scattered signal to a lesser degree.

### **Calculation of Experimental Photon Arrival Rate**

The voltage as a function of time waveform obtained on the oscilloscope represents the total scattered intensity recorded at the photomultiplier tube per pulse.

Figure 5-6 shows a typical waveform of a burst seen on the oscilloscope. The waveform is recorded at a downstream distance of 4 nozzle diameters with no flow fluid.

Integrating this waveform using equation 5.5 gives the total scattered intensity per pulse ( $V_{PMT}$ )

$$V_{PMT} = \sum_{i=0}^{i=100} 0.5(V_i + V_{i+1})(0.1) \quad (5.5)$$

where (i) represents the time scale from 0 to 100 microseconds varied in steps of 0.1 each.

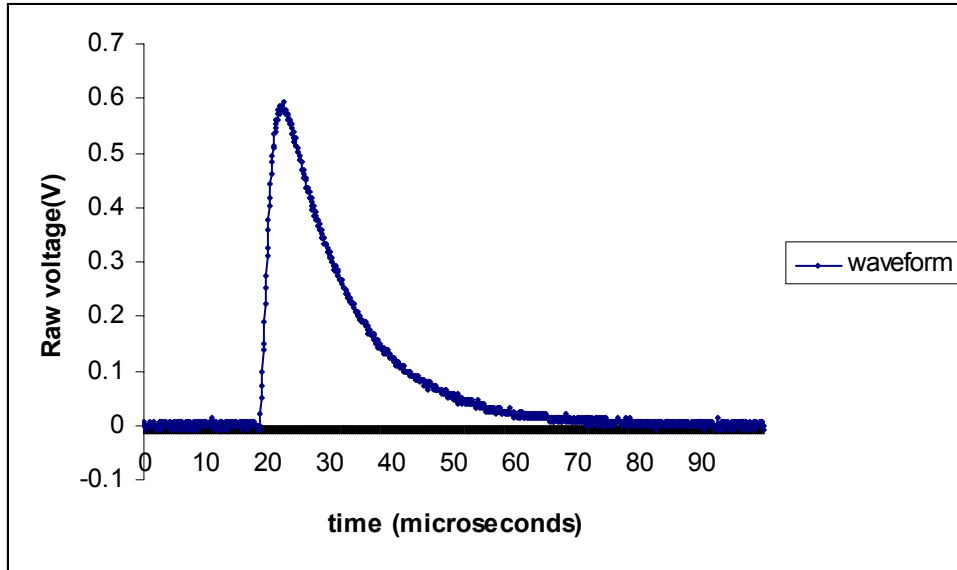


Figure 5-6. Typical waveform of a burst seen on the oscilloscope (Downstream distance of 4 nozzle diameters, no flow fluid)

The Photomultiplier tube calibration constant (CPMT) at the wavelength of 532 nm is found to be 121 V/nW from the manufacturers specifications. The measurements are done using the pulsed ND:YAG laser at 6 different helium concentrations of 0, 20, 40, 60 80 and 100% using the ¼" diameter nozzle. As discussed in buoyant jet theory (Figure 3-5) the flow fluid (helium) concentration can be predicted in the shear layer for a combination of downstream distances and radial distance ( $r/z$ ). The downstream distance ( $z$ ) is fixed at 2 nozzle diameters. From equation 3.23 it is seen that for a fixed value of  $z$ , the radial distance ( $r$ ) can be calculated if the concentration  $C$  is known since the centerline concentration of the flow fluid ( $C_{cl}$ ) is known using equation 3.25 and the concentration of flow fluid ( $C_a$ ) in the ambient is 0%.

$$\frac{C - C_a}{C_{cl} - C_a} = \exp [-K_c(r/z)^2] \quad (3.23)$$

Thus for 6 different values of  $C$  (0, 20, 40, 60, 80 and 100), the measurements are made for the corresponding values of radial distance( $r$ ) obtained from equation 3.23.

Figure 5-7 shows the values of radial distance  $r$  where the measurements are made for each value of  $C$ .

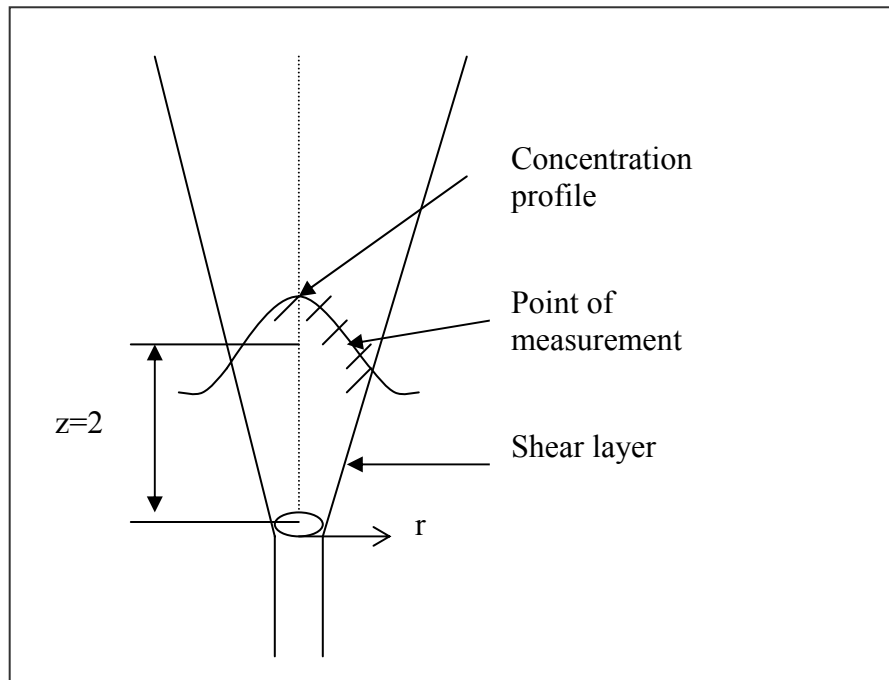


Figure 5-7. Figure shows points in shear layer where measurements are made corresponding to each value of  $C$  using pulsed Nd:YAG laser and  $\frac{1}{4}$ " nozzle at a downstream distance of 2 nozzle diameters.  $Re = 500$ ;  $Fr = 290$ .

For each measurement the integrated area under the voltage- time curve on the oscilloscope represents the total scattered signal per burst. Equation 5.6 is used to convert the voltage recorded for each measurement into scattered signal in photons per pulse.

$$I_{\text{experimental}} = V_{\text{PMT}} \lambda / C_{\text{PMT}} h c \quad (5.6)$$

Figure 5-8 shows the comparison of the experimental and theoretical photon arrival rates for varying percentages of helium.

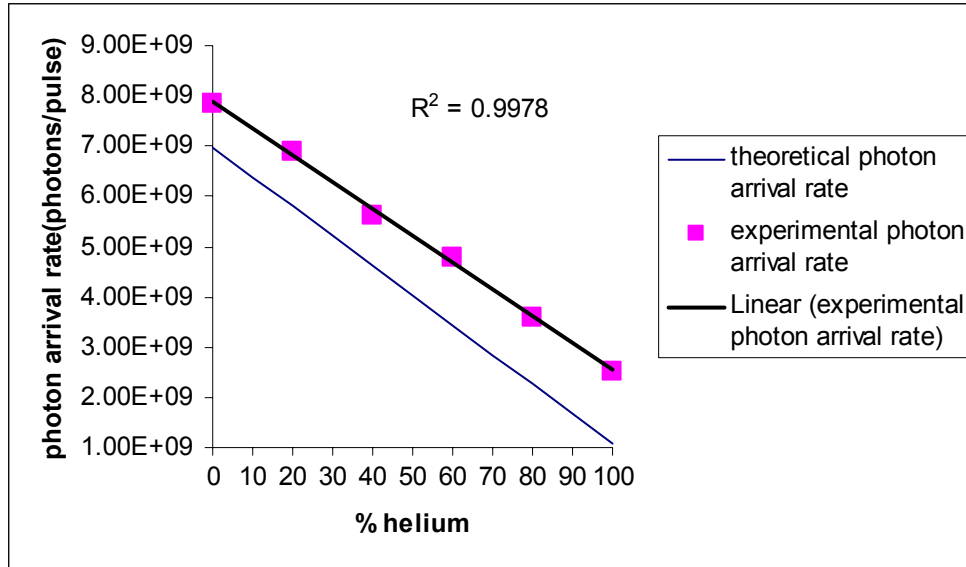


Figure 5-8. Comparison of experimental and theoretical photon arrival rates.

The experimental and theoretical photon arrival rates are of the same order of magnitude with a maximum error of 57.3% for the case of 100% helium and a minimum error of 11.3% for the case of 0% helium. A linear regression of the experimental photon arrival rate gives a coefficient of 0.99 indicating a constant additional factor(s) contributing to the error independent of percent helium. This constant error can be attributed to 1. Background glare, which is at the same wavelength as that of scattered signal. 2. Deviation of optical efficiency of each collection surface from the assumed value of 90%. 3. Ambient air in control volume at jet edges.

### Data Analysis Techniques

As previously stated for each burst the scattered signal from the photomultiplier tube is recorded as a voltage-time curve on the oscilloscope. Two techniques of analyzing the recorded voltage are considered. The Nd:YAG pulse laser with the ¼" nozzle is used for both techniques and the flow fluid is pure helium for both cases.

### Integrated area method

Initially a set of 1000 data points per burst are captured from the oscilloscope and the integrated area under the voltage as a function of time curve is computed. For the measurements, the downstream distance is 2 nozzle diameters, Reynolds number is 500 and Froude number is 290. The measurements are done in the shear layer of the leak at a radial position corresponding to 60% helium concentration as shown in figure 5-7. This is because the maximum variation of recorded voltage is expected to be in the shear layer edge since the intermittency of the turbulence is maximum.

This procedure was repeated for a set of pulses at the same nozzle position shown in figure 5-7 until the areas converged. Figure 5-9 shows the convergence studies for the area.

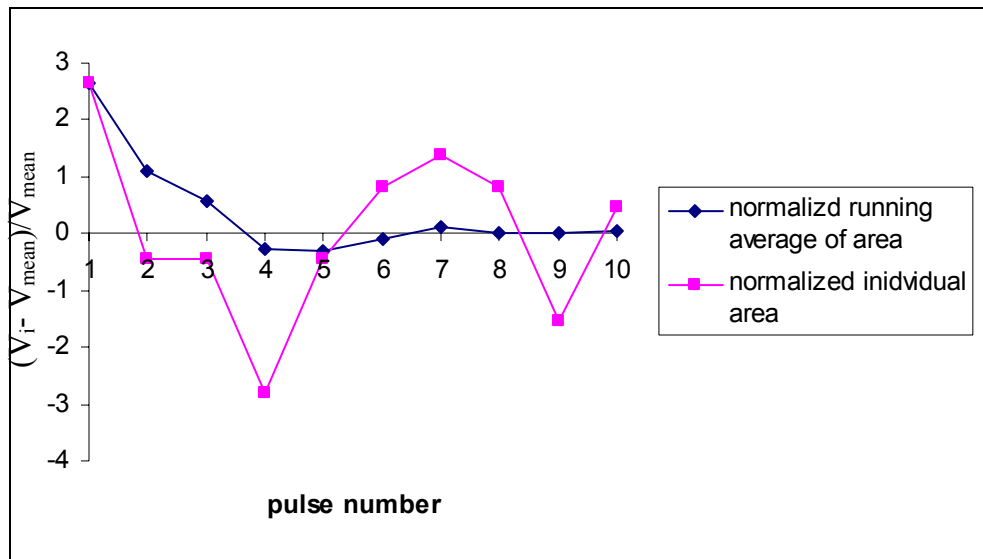


Figure 5-9. Convergence studies of normalized area and averaged area shows that the area converged in 10 pulses.

Series 1 represents the running average of the integrated area normalized with respect to the mean of 10 pulses. As seen from the graph, for a measurement in the shear layer a set of 10 pulses are enough for convergence. The maximum percent variation of

any individual area from the mean is 3% and the maximum percent variation of the running average of area from the mean is 2.6%.

### Peak Voltage Method

Two studies are undertaken to validate the use of peak voltage rather than integrated area as a repeatable and reproducible data measurement technique. A convergence study is also done to determine the number of peaks required for data measurement. These studies are carried out using the pulsed Nd:YAG laser with the 1/4" nozzle.

**Study 1.** For four downstream positions ( $z$ ) of 2, 4, 6, and 8 nozzle diameters the waveform is recorded along the jet centerline ( $r=0$ ) as seen in Figure 5-10.

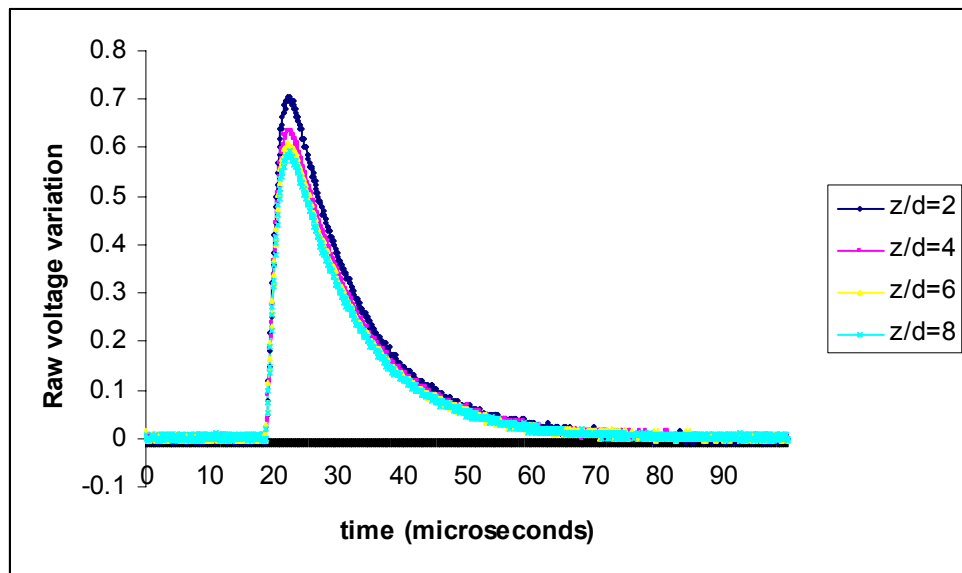


Figure 5-10. Waveform with varying glare at four downstream locations.

All four measurements are done in room air with no helium flowing through the nozzle. In this case we expect that the Rayleigh and Mie scattering signals are constant and the only variable in each case was the glare from the nozzle.

All four waveforms were normalized with the corresponding peak as shown in figure 5.11. It is seen that all four waveforms fall on top of each other and it is impossible to distinguish between them. A four way cross correlation analysis of the waveforms was done using the following relation

$$r_{x-y} = \frac{\sum(x_i - \bar{x})(y_i - \bar{y})}{\sqrt{((x - \bar{x})/N_d)^2} \sqrt{((y - \bar{y})/N_d)^2}} \quad (5.7)$$

The cross correlation coefficient was 99.7%. The high cross correlation coefficient supports the hypothesis that the peak voltage contains sufficient information of each waveform.

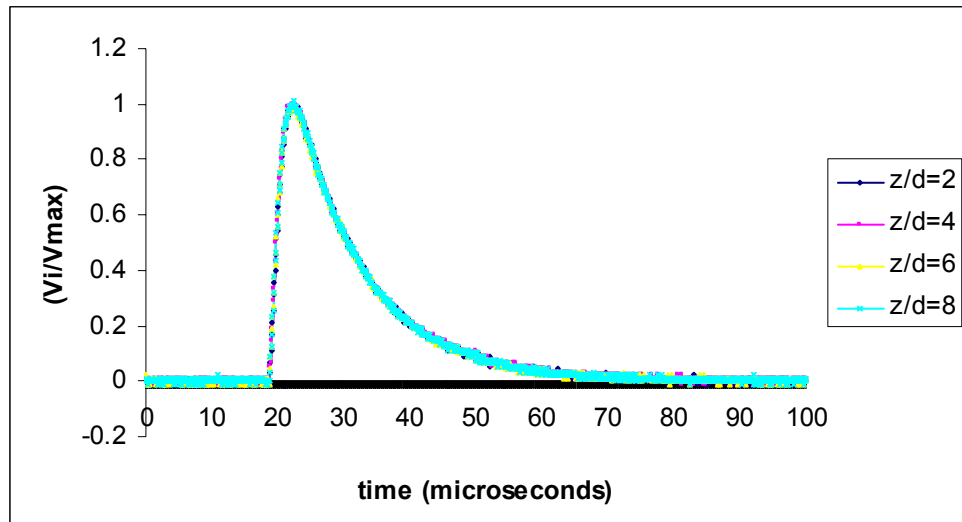


Figure 5-11. All four waveforms normalized with their individual peaks to remove glare, the waveforms are indistinguishable.

**Study 2.** In this study, a correlation analysis of the peak voltage and the corresponding integrated area is done for 10 pulses at the same nozzle position in the shear layer as that used with the integrated area studies above (Figure 5.7). The flow fluid is 100% helium and the Reynolds and Froude numbers are 500 and 290 respectively and

radial position corresponding to 60% helium concentration. The downstream distance is 2 nozzle diameters. The correlation coefficient is 99.3% which again supports the relation between peak and area for a given pulse.

**Peak Convergence Study.** From the previous two studies it is established that the peak contains all necessary information about the waveform and the peak and area are related. The convergence study is undertaken to establish the number of pulses required for convergence. The downstream distance is 2 nozzle diameters and the Reynolds and Froude numbers are 500 and 290 respectively for 100% helium. The measurements are done in the same position in the shear layer of the leak as for the previous two cases of integrated area and comparison of integrated area and peak (Figure 5.7) (radial position corresponding to 60% helium concentration. The average peak voltage is recorded after the 1st, 100th, 200th, 300th, 400th and 500th pulse. Table 5.2 lists the voltage recorded after each measurement. Column 3 of the table gives percent variation between two consecutive values of recorded voltage.

Table 5-2. Shows that average peak voltage recorded after 300 pulses in shear layer is a converged mean.

Pulse Number	Average peak voltage ( $V_i$ ) (mV)	$(V_i - V_{i-1})/V_i$
0	550	
100	576	4.7%
200	564	2.1%
300	559	0.88%
400	563	0.76%
500	558	0.89%

As seen from table 5.1 the variation between average peak voltage is less than 1% if the peak voltage was recorded after 300 pulses. Also these measurements are carried out in the edge of the shear layer of the jet where the fluctuations in the flow are

maximum. Hence it is concluded that for any nozzle position, recording the average peak voltage after 300 pulses is a reliable data measurement technique.

### **Analysis of Recorded Data**

Figure 5-6 shows the comparison between the predicted (theoretical) and the measured (experimental) photon arrival rates. As stated earlier these studies are carried out using the pulsed Nd:YAG laser with a ¼" diameter nozzle at a downstream distance of 2 nozzle diameters. This section discusses the variation of peak voltage and standard deviation of the recorded voltage for the following four cases:

- Argon-ion laser with a ½" diameter nozzle at downstream distances of 2 and 4 nozzle diameters for pure helium for 90° scattering scheme.
- Pulsed Nd:YAG laser with a ¼" diameter nozzle at downstream distances of 2, 4, 6 and 8 nozzle diameters for pure helium for 90° scattering scheme.
- Pulsed Nd:YAG laser with a ¼" diameter nozzle at downstream distances of 2 and 4 nozzle diameters for a mixture of 20% helium and 80% nitrogen for 90° scattering scheme.
- Pulsed Nd:YAG laser with a ¼" diameter nozzle at downstream distances of 2, 6, 10 and 16 nozzle diameters for pure helium in back scatter.

The nozzle was traversed in the radial (r) direction as discussed in chapter 4 for the 90° scattering scheme and in the (y) direction for the back scatter scheme.

#### **Case I: Argon-ion laser**

##### **Peak voltage variation**

Initially the measurements were carried out using the argon-ion laser ( $\lambda = 488 \text{ nm}$ ) at two downstream distances of 2 and 6 nozzle diameters. The nozzle diameter of ½" is used with the argon-ion laser and the flow fluid is pure helium. The Reynolds number of the leak is 500 and the Froude number is 35. the nozzle traverse distance for each measurement at each downstream position were calculated as discussed in Chapter 3. Three sets of measurements were done at each downstream position. Figure 5-11 shows the average of the normalized peak for all 3 measurements. Also shown are the error bars

at both downstream locations corresponding to the standard deviation of each measurement point. The x-axis is the nozzle traverse distance ( $r$ ) in mm. As seen from the figure, the scattered voltage reaches a minimum value of zero at the jet centerline for both downstream distances. Also the voltage variation inside the shear layer is visible. Hence due to the presence of helium in the shear layer, there is a fall in voltage inside the shear layer. As the downstream distance increases, the jet spreads out and the fall occurs over a wider radius.

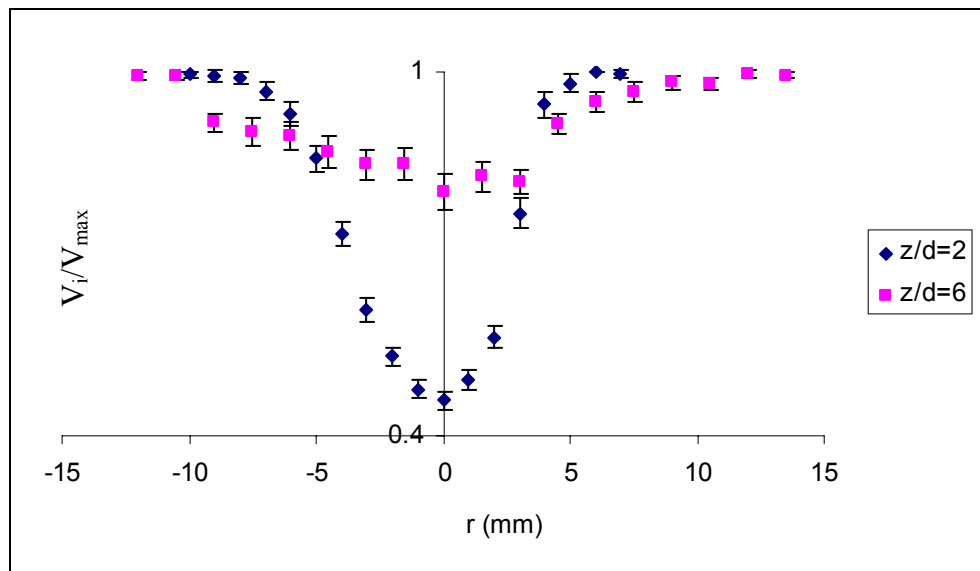


Figure 5-12. Voltage variation for Argon-Ion laser shows that there is a fall in voltage in presence of helium;  $\frac{1}{2}$ " nozzle at two downstream distances;  $Re = 500$ ;  $Fr = 35$ .

As seen from figure 5-12, the fall in peak voltage at the jet centerline which corresponds to 100% helium. Also, the fall in voltage occurs only in the presence of helium. At the ambient where there is no effect of flow fluid on the recorded voltage, the voltage remains constant. The fall in voltage in presence of helium occurs because 1. Helium molecules have a scattering cross section which is 0.015 times the cross section

of the surrounding air molecules. 2. Molecules of the flow fluid displace some aerosols in their path which are Mie scatters. Hence there is a fall in the intensity of scattered light

### Normalized peak voltage variation.

The raw peak voltage was normalized with the centerline voltage  $(V_i - V_a)/(V_{cl} - V_a)$  as shown in figure 5-13. The normalized concentration profile plotted in chapter 3 is also shown as a function of  $r/z$ . From figure 5-13 it is seen that the voltage variation follows a similar Gaussian distribution as that of well established normalized concentration profile of a axisymmetric vertical buoyant jet.

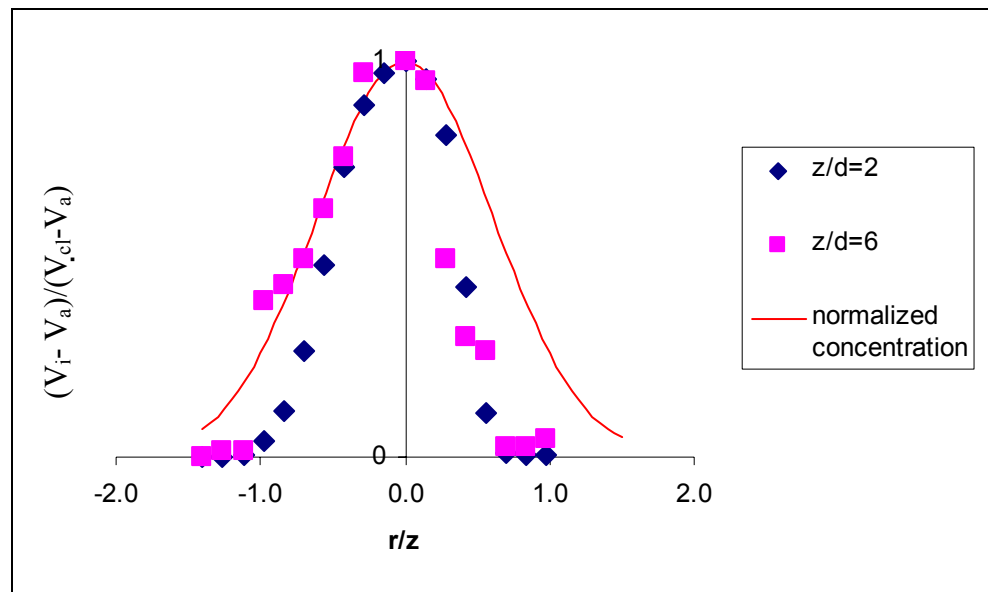


Figure 5-13. Normalized peak voltage variation for argon-ion laser for pure helium;  $Re=500$ ;  $Fr=3.5$ ; nozzle diameter =  $\frac{1}{2}$  "

### Standard deviation profiles

Figure 5-14 shows the variation of the normalized standard deviation ratioed to the centerline voltage  $\sigma/(V_{max} - V_{cl})$  for the downstream distance of 2 nozzle diameters. The downstream distance of 2 nozzle diameter represents the near field regime of the buoyant jet. It is seen that inside the potential core, the standard deviation falls as expected.

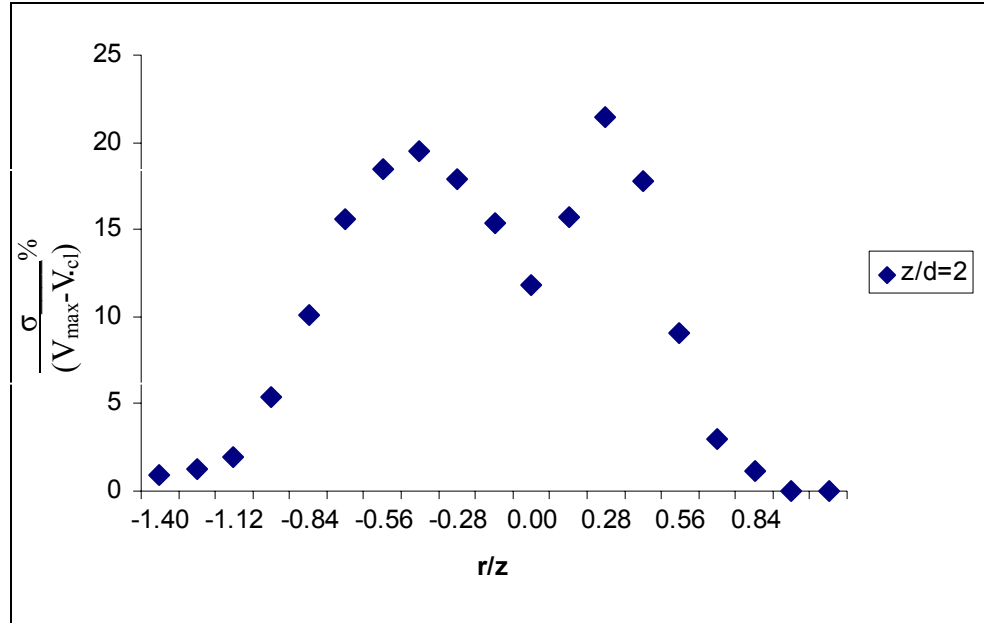


Figure 5-14. Percent standard deviation variation for near field case showing the reduced fluctuation in the potential core.

Figure 5-15 shows the variation of the normalized standard deviation of the data radioed to the centerline standard deviation for the far field case after the shear layers have coalesced.

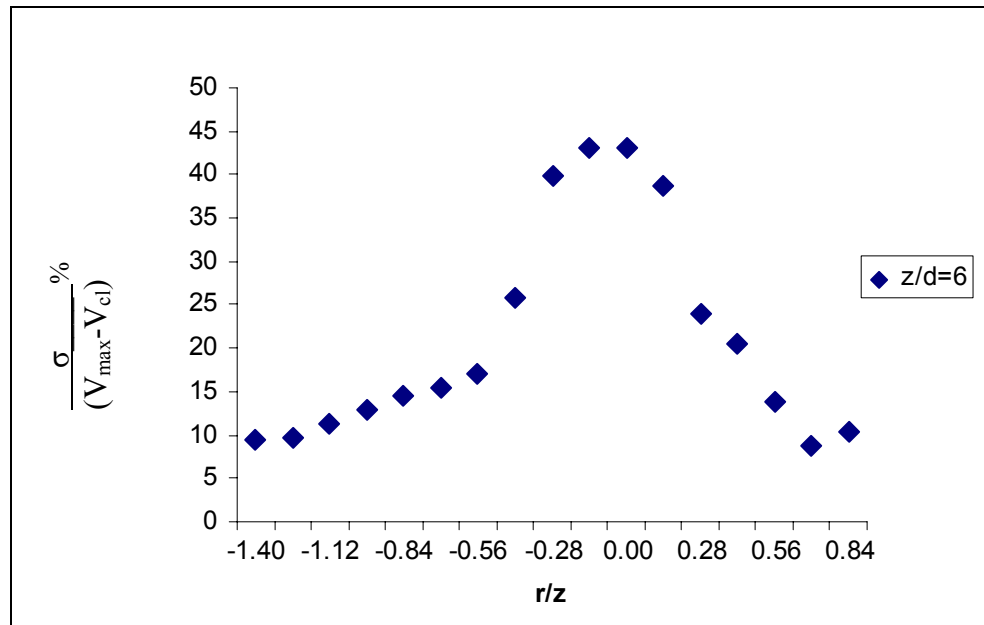


Figure 5-15. Percent standard deviation for far field case after shear layers have coalesced.

The percent standard deviation is above the typical maximum variation of 30%. A possible reason for this is there is an additional factor of Mie scattering contributing to the increased standard deviation of the recorded voltage.

## Case II: Pulsed Nd:YAG laser ; pure helium

### Peak voltage variation.

Figure 5-16 shows the variation of raw peak voltage with respect to the nozzle position for pure helium for the downstream distances of 2, 4, 6 and 8 nozzle diameters for the pulsed Nd:YAG laser ( $\lambda=532$  nm) using the  $\frac{1}{4}$  " nozzle. The Reynolds number is 500 and Froude number is 290. As seen from the graph, for each individual downstream distance the voltage tends to remain constant outside the shear layer (ambient) due to absence of helium. As observed with the argon-ion laser, the fall in voltage occurs over a wider radius as the jet spreads out. Also the minimum voltage is recorded at the jet centerline.

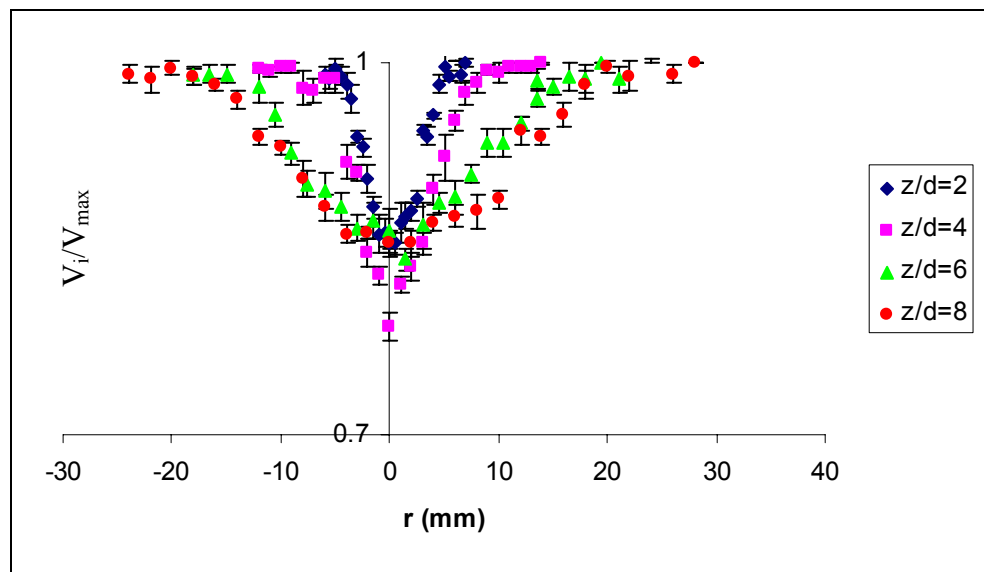


Figure 5-16. Voltage variation for pulsed Nd:YAG laser shows a similar profile of fall in voltage in presence of helium;  $Re= 500$ ;  $Fr=290$ ; nozzle diameter =  $\frac{1}{4}$  "

### Normalized Peak Voltage Variation

Figure 5-17 shows the variation of the normalized peak voltage for all four downstream distances for the pulsed Nd:YAG laser for the case of pure helium. Also shown is the theoretical normalized concentration profile plotted in chapter 3 as a function of  $r/z$ .

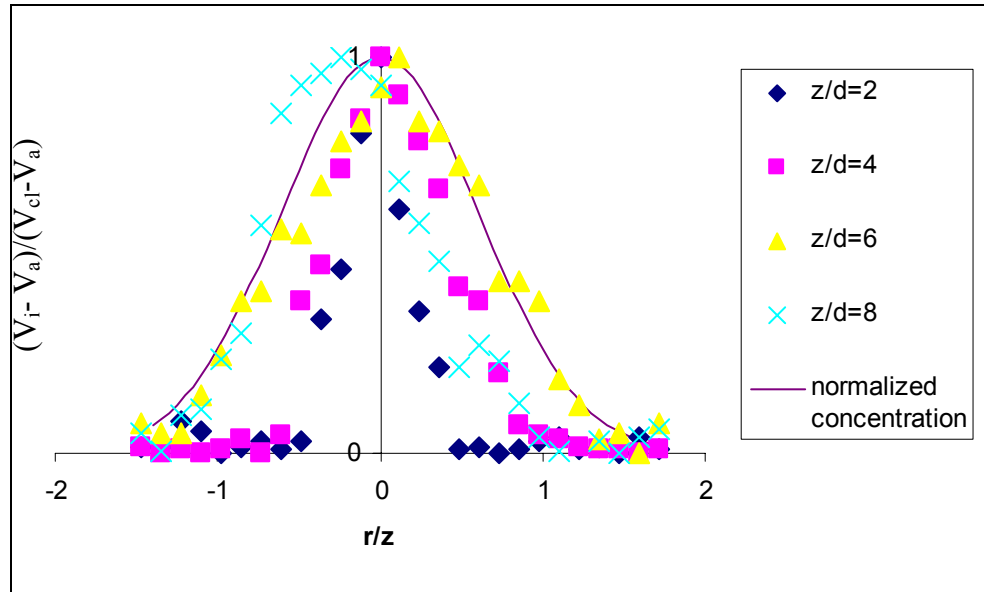


Figure 5-17. Normalized peak voltage variation for Nd:YAG laser for pure helium;  $Re=500$ ;  $Fr=290$ ; nozzle diameter =  $\frac{1}{4}$  "

### Standard deviation profiles

Figure 5-18 shows the standard deviation profiles for all four downstream distances of 2, 4, 6 and 8 nozzle diameters. Comparing figure 5-18 with the standard deviation profiles for the Argon-ion laser (figures 5-14 and 5-15), it is seen that the standard deviation variation is less distinct for the Nd:YAG laser. A possible reason for this could be the effect of the relative size of beam and nozzle (leak) diameters. The beam diameter for the argon ion laser is 1/10th the diameter of the nozzle whereas for the pulsed laser it was 1.2 times the nozzle diameter (Figure 5-19). This factor was an additional variance for the pulsed laser.

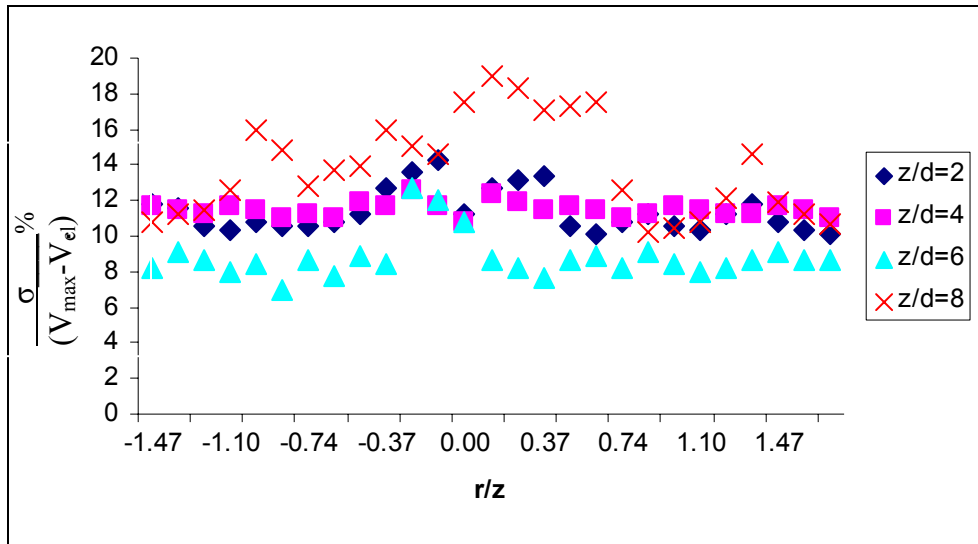


Figure 5-18. Standard deviation variation for Nd:YAG laser for pure helium;  $Re=500$ ;  $Fr=290$ ; nozzle diameter =  $\frac{1}{4}$  "

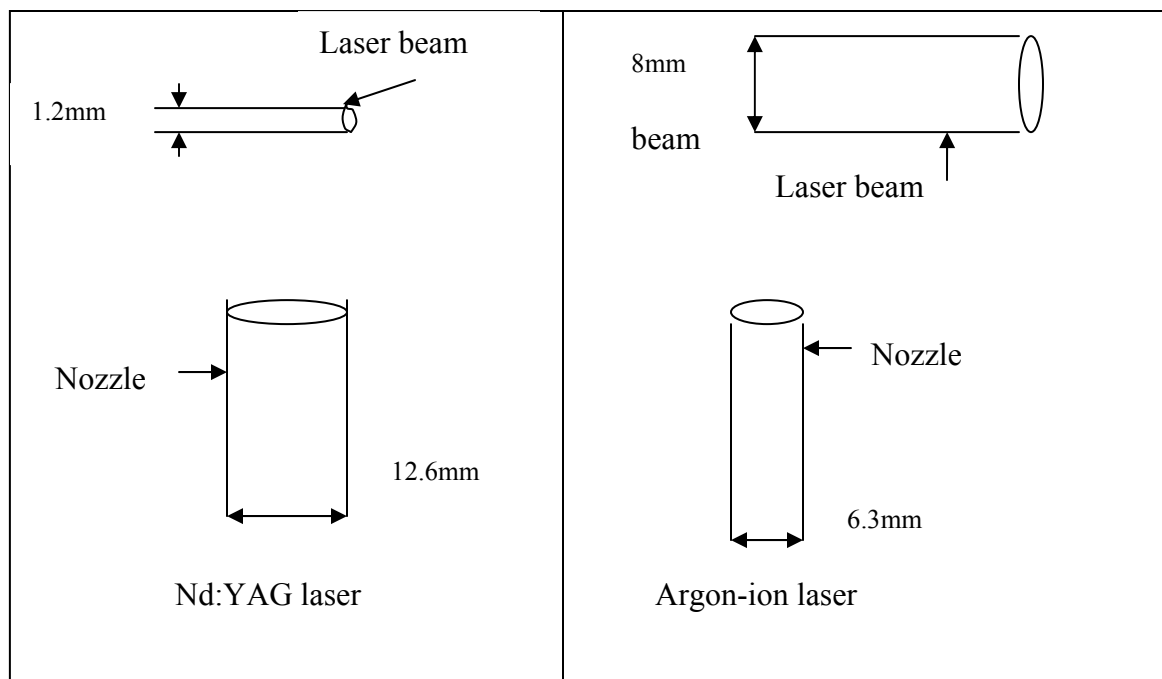


Figure 5-19. Relative size of beam and leak diameter for the Argon-ion and pulsed Nd:YAG laser.

### Case III: Pulsed Nd:YAG laser; 20%helium ,80% nitrogen

#### Peak Voltage Variation

Figure 5-20 shows the variation of peak voltage for a mixture of 20% helium and

80% nitrogen for a downstream distance of 2 and 4 nozzle diameters for the pulsed Nd:YAG laser. This mixture of helium and nitrogen matches the scattering cross section of hydrogen as discussed in Chapter 3 and hence the amount of light scattered by the mixture is expected to be identical to that of Hydrogen. The Reynolds and Froude number were 500 and 515 respectively.

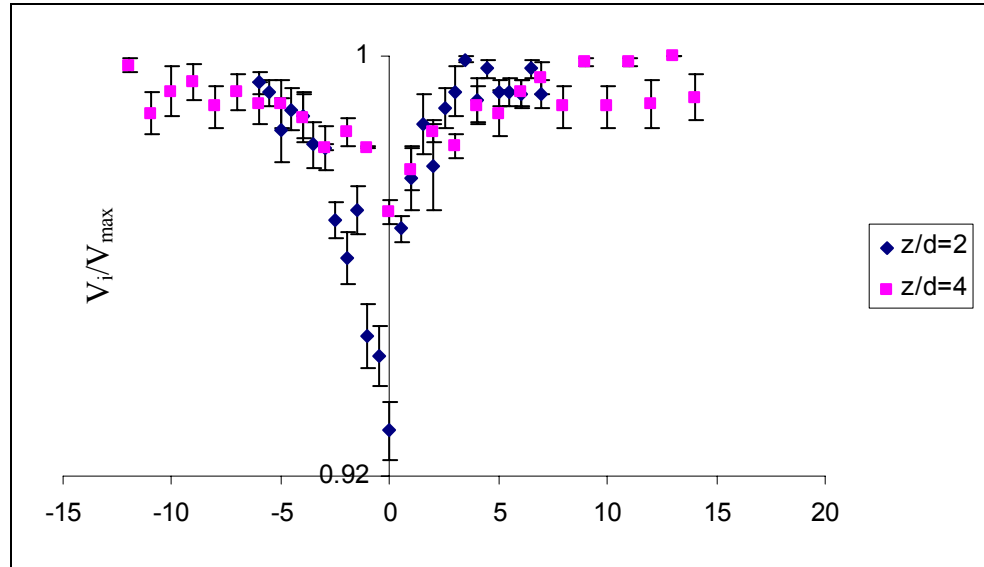


Figure 5-20. Voltage variation for the pulsed Nd:YAG laser for the mixture of helium and nitrogen shows that there is a fall in voltage; nozzle diameter  $\frac{1}{4}$ " ;  $Re=500$ ,  $Fr = 515$ .

The fall in voltage from figure 5-20 is 30 mV (6%) for the downstream distance of 2 nozzle diameters. The fall in voltage for  $z/d=2$  for the case of 100% helium is 155 mV (30 %) as seen in figure 5-16.

#### **Normalized peak voltage variation.**

Figure 5-21 shows the normalized peak variation for the mixture at the downstream distances of 2 and 4 nozzle diameters.

A comparison with the normalized concentration shows that the two profiles are similar.

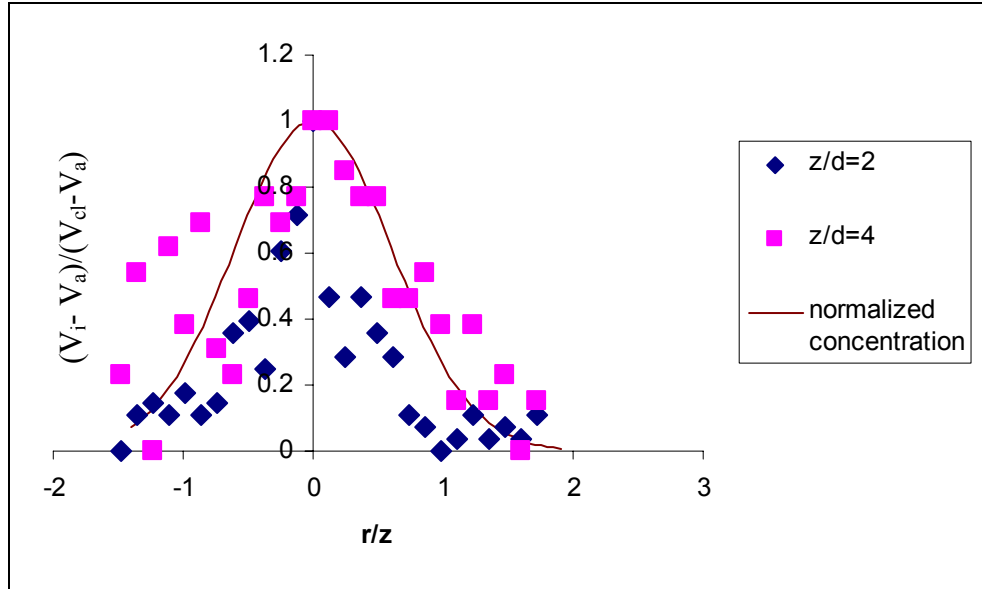


Figure 5-21. Normalized peak voltage variation for Nd:YAG laser ;  $Re= 500$ ;  $Fr=515$ ; nozzle diameter =  $\frac{1}{4}$  " for a mixture of helium and nitrogen to simulate the optical properties of nitrogen.

#### Standard Deviation Profiles.

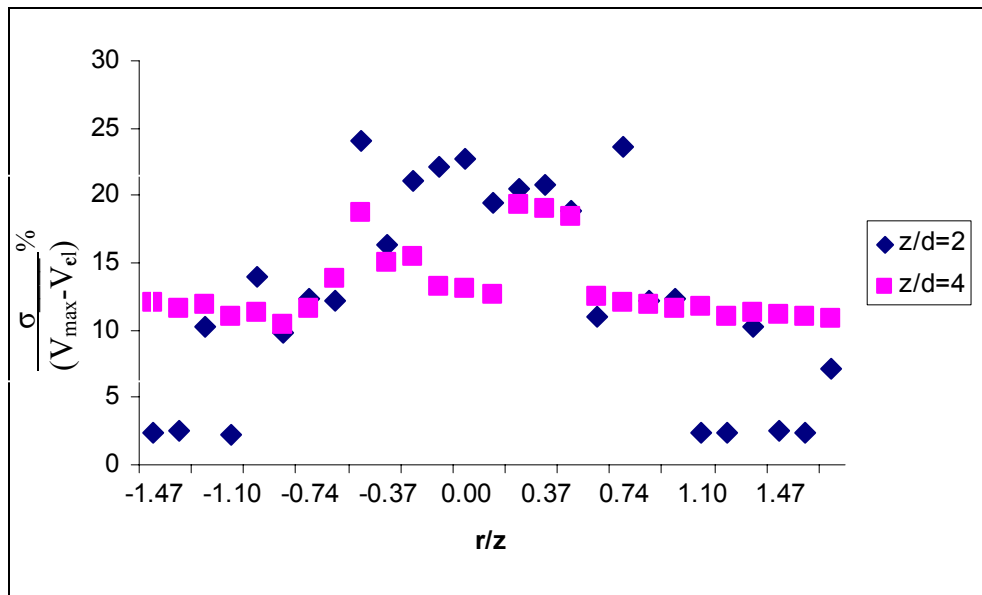


Figure 5-22. Percent standard deviation variation for Nd:YAG laser ;  $Re= 500$ ;  $Fr=515$ ; nozzle diameter =  $\frac{1}{4}$  " for a mixture of helium and nitrogen to simulate the optical properties of nitrogen

The standard deviation profiles of the mixture for both downstream distances of 2 and 4 nozzle diameters are shown in figure 5-22. The standard deviation for the mixture

is more than the standard deviation of pure helium for the two distances. The presence of two flow fluids (helium and nitrogen) shows in the increased standard deviation.

### Measurements in Backscatter

The principal issue in backscatter is distinguishing between the scattered signal and beam dump glare. Figure 5-23 is a schematic of the backscatter geometry represented on a time scale. The time difference between the scattered beam from the nozzle and reflected beam from the beam dump is approximately 20ns. Thus the photomultiplier tube should be able to distinguish between the two signals 20 ns apart. The minimum bandwidth of the photomultiplier tube required is 5 MHz. It was impossible to distinguish between the two signals using the Hammamatsu tube. (Bandwidth 23 KHz).

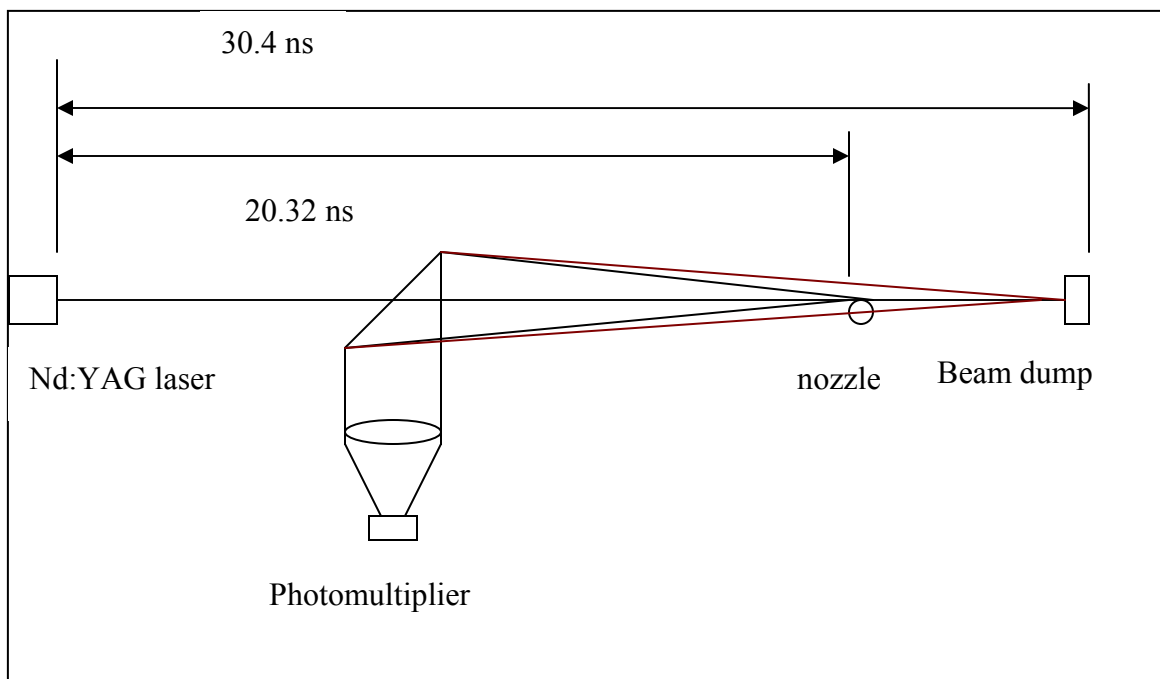


Figure 5-23. Schematic of backscatter on a time basis shows separation between beam dump glare and scattered signal from the nozzle.

The waveform seen on the oscilloscope contained both the beam dump glare and the scattered signal. In order to distinguish between the signal and glare the

measurements with helium for a typical nozzle position was normalized with a measurement without helium for the same nozzle position. Since the measurements were done in backscatter, the nozzle was traversed in a direction perpendicular to that of the beam(y-direction). Figure 5-24 shows the data in backscatter.

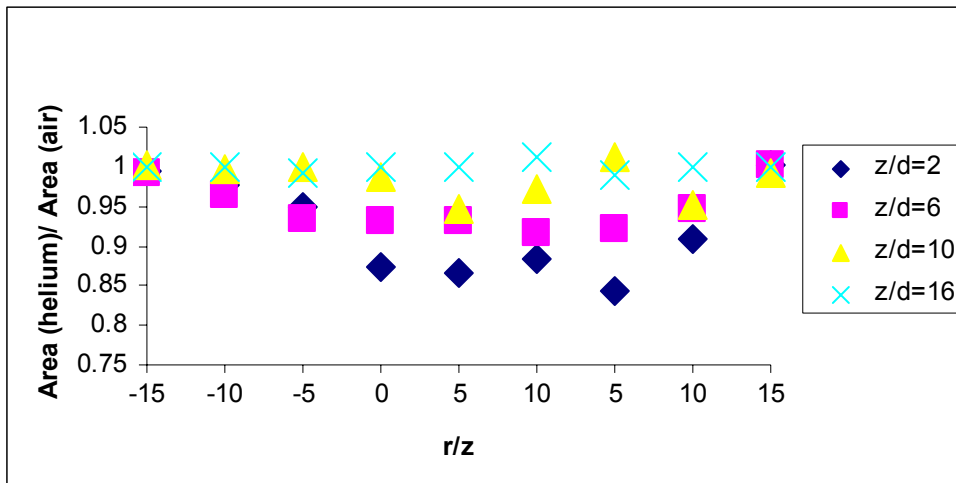


Figure 5-24. Normalized area variation shows a reduction in scattered intensity in presence of helium (backscatter); Nozzle diameter =  $\frac{1}{4}$ " ; Re =500; Fr = 290

There is a fall in the normalized area in the presence of helium near the jet centerline for all downstream distances. For the case of downstream distance of 2 nozzle diameters, the fall in normalized area is about 0.15 V (15%). For the 90° scattering scheme for the pulsed Nd:YAG laser, the fall in voltage is approximately 30% (Figure 5-16) and 50% for the Argon-Ion laser for the downstream case of 2 nozzle diameters for pure helium (Figure 5-12). The control volume for the backscatter geometry is defined by the 6mm diameter beam and the pulse width of 5 ns (1.5m) ( $4.29E-5m^3$ ). For the 90° scattering scheme, the control volume is defined by the 6mm diameter beam and the 0.015mm optical slit ( $4.29E-3m^3$ ) for the Nd:YAG laser, and 1mm diameter beam and the 0.15mm optical slit for the Argon-Ion laser. ( $7.05E-12m^3$ ). The leak diameter for the pulse laser is  $\frac{1}{4}$ " whereas for the Argon-Ion laser its  $\frac{1}{2}$ ". Thus for the 90° scattering

geometry for both Argon-Ion and Nd:YAG cases, the leak occupies 100% of the control volume whereas for the backscatter geometry the leak occupies only 0.6% of the control volume as seen from table 5-3.

Table 5-3. Control volume to leak diameter ratio for all three cases shows that the ratio is far less for backscatter than 90° scattering.

Geometry	Nozzle Diameter (D)	Control Volume(CV)	CV/D (percent)
Backscatter,Nd:YAG	6.35E-3 m	4.29E-5m <sup>3</sup>	0.6
90° Nd:YAG	6.35E-3 m	4.29E-5m <sup>3</sup>	100
90° Argon-Ion	12.7E-3 m	4.29E-5m <sup>3</sup>	100

This might have lead to the lesser fall in intensity of scattered light in the presence of helium for backscatter geometry.

## CHAPTER 6 CONCLUSIONS

The primary objective of this study is to establish the feasibility of laser induced light scattering as a leak detection technique for hydrogen. There are two primary reasons that support this objective.

1. The fall in voltage at the centerline of the leak indicating reduced scattered intensity both in the presence of pure helium ( $\sigma_{\text{Helium}} = 0.015 \sigma_{\text{Air}}$ ) and a mixture of 20% helium and 80% nitrogen ( $\sigma_{\text{Mixture}} = \sigma_{\text{Hydrogen}} = 0.23 \sigma_{\text{Air}}$ ) 2. Standard deviation in excess of 30% for pure helium (argon ion laser). Both of these were due to the reduced intensity of Rayleigh scattering by helium molecules.

The theoretical studies of Mie scattered intensity show that the Mie signal is the same order of magnitude for the laboratory and maritime particle distributions. This result is important for field measurements as the effect of Mie scattering on the total signal would be approximately the same. Initially it was thought that the fall in voltage would be amplified due to the Mie scatters. However, from the theoretical study it was seen that Mie signal is less than the Rayleigh signal. Hence the lack of Mie scatters in the control volume reduces the fall in voltage in the presence of Rayleigh scattering due to helium and nitrogen molecules.

Concentration measurements in the presence of Mie scattering have been successfully done in the lab environment. The backscattering scheme is used principally to test the feasibility of this technique for field measurements. Since for laboratory measurements the scattered signal from the photomultiplier tube and the reflection from

the beam dump are only 40 ns apart, it was impossible to distinguish between the two signals for the photomultiplier tube used for the experiments. This lack of temporal discrimination severely limits the overall signal to noise ratio for this configuration. The signal to noise ratio can be improved with better overall temporal response devices.

A fall in voltage at the centerline of the flow is observed for both pure helium and the mixture of 20% helium and 80% nitrogen for all four downstream distances. This indicates that a leak could be detected at downstream distances as low as 8 nozzle diameters. Also leak detection is feasible when taken in context of the overall full field concentration distribution.

### **Future Work**

- In order to determine the effect of background light, a dual line detection system should be used.
- A study to determine the polarization effect of the incident beam on the scattered signal should be done.

## LIST OF REFERENCES

- Becker H, Hottel H, Williams G, Light scatter technique for the study of turbulent mixing, *Journal of Fluid Mechanics*, Nov 1967, vol. 30 (2), pp 259-284
- Bohren C, Huffman D, 1983, *Absorption and scattering of light by small particles*, Wiley, New York.
- Bryner N, Pitts W, A Rayleigh Light scattering technique for investigation of free jets and plumes, *Review of Scientific Instruments*, 1992, vol. 63 (7), pp 3629-2635
- Chen C, Rodi W, 1980, *HMT the science and applications of heat and mass transfer*, vol. 4, Pergamon Press, Oxford.
- Dave J, 1970, Scattering of electromagnetic radiation by a large, absorbing sphere. *IBM J. Res. Dev.* 1969, vol. 13(3), pp 302-313.
- Dibble R, Hollenbach R, Rambach G, Temperature measurements in turbulent flames via Rayleigh scattering, 1980, *American Chemical Society*, pp 435-441.
- Dyer T, Rayleigh scattering measurements of time resolved concentration in a turbulent propane jet, 1979, *AIAA Journal* , vol. 17(8), pp 912-914
- Graham S, Grant A, Jones J, Transient molecular concentration measurements in turbulent flows using Rayleigh light scattering, 1974, *AIAA Journal*, vol. 12(8), pp 1140-1142
- Horton J, Peterson J, Transient temperature measurements in an ideal gas by using laser induced Rayleigh light scattering, August 1999, *Review of Scientific Instruments*, vol. 70(8), pp 3222-3226.
- Kerker M, 1969, *The scattering of light and other electromagnetic radiation*, Academic Press, New York.
- Long M, Chu B, Chang R, Instantaneous two dimensional gas concentration measurements by light scattering, *AIAA Journal*, September 1981, vol. 19(9), pp 1151-1157.
- Matthew A, Peterson J, Flow visualizations and transient temperature measurements in an axisymmetric impinging jet rapid thermal chemical vapor deposition reactor, June 2002, *Journal of Heat Transfer*, vol. 124, pp 564-570
- McCartney E, 1976, *Optics of the atmosphere*, Wiley, New York.

- Muller-Dethlefs K, Weinberg F, Burning velocity measurements based on laser Rayleigh scattering ,1979, Seventeenth symposium on combustion, vol. 27(2), pp 985-992.
- Otugen M, 1997, Nd:YAG laser based dual line Rayleigh scattering system, AIAA Journal vol. 35(5), pp 776-780.
- Prahl S, [http://omlc.ogi.edu/calc/mie\\_calc.html](http://omlc.ogi.edu/calc/mie_calc.html) , Last accessed :10/20/2004, Oregon Medical Laser Center.
- Pitts W, Kashiwagi, 1983, The application of laser induced Rayleigh light scattering to the study of turbulent mixing, Journal of Fluid Mechanics, vol. 141, pp 391-429.
- Pitz R, Cattolica R, Robben F, Talbot L, Temperature and Density in a Hydrogen Air Flame from Rayleigh scattering, 1976, Com. Flame, vol. 27(3), pp 313-320.
- Robben F, Comparison of density and temperature using Raman scattering and Rayleigh scattering using combustion measurements in jet propulsion systems,1975, Proceedings of a project SQUID workshop, Purdue University. pp 179-195.
- Rodi W, 1982, HMT the science and applications of heat and mass transfer, Pergamon Press, Oxford
- Rosenweig R, Hottel H, Williams G, Smoke scattered light measurements of turbulent concentration fluctuations, Chem. Eng. Science, 1961, vol. 15(1,2), pp 111-129.
- Schlichting H, 1979, Boundry layer theory, McGraw Hill Series in Mechanical Engineering, New York
- Shaughnessy E, Morton J, Laser light scattering measurements of particle concentration in a turbulent jet. Journal of Fluid Mechanics, April 1977, vol. 80(1), pp129-148.
- Wiscombe W, 1989, Improved Mie scattering algorithms, Applied Optics, 1980, vol. 19(9), 1505-1509

## BIOGRAPHICAL SKETCH

Sameer Paranjpe finished his undergraduate degree in mechanical engineering from the University of Bombay in 2002. He is pursuing his master's degree in mechanical engineering at the University of Florida. He has been a research assistant under Dr. Jill Peterson since August 2002.